TECHNISCHE UNIVERSITÄT DRESDEN

Fakultät Maschinenwesen, Institut für Strömungsmechanik, Professur für Strömungsmechanik

Diplomarbeit

Adaptation and validation of the σ-model for large-eddy simulations with the discontinuous Galerkin method

vorgelegt zur Erlangung des akademischen Grades ”Diplomingenieur”

Yang Liu

geboren am 22. August 1995

in Shandong

eingereicht am 15. Juni 2021

1. Gutachter Prof. Dr.-Ing. habil. J. Fröhlich

2. Gutachter PD Dr. J. Stiller

TECHNISCHE UNIVERSITÄT DRESDEN

D – 2281

Fakultät Maschinenwesen, Institut für Strömungsmechanik, Professur für Strömungsmechanik

Aufgabenstellung zur Diplomarbeit

Name: **Yang Liu** **Matr.-Nr.: 4812613**
Studienrichtung Luft- und Raumfahrttechnik

Thema: **Adaptation and validation of the σ-model for large-eddy simulations with the discontinuous Galerkin method**

(Anpassung und Validierung des σ-Modells für Large-Eddy-Simulationen mit der Diskontinuierlichen Galerkin-Methode)

Zielsetzung:

The discontinuous Galerkin (DG) method gains increasing attention in the fluid dynamics community. In recent works it is claimed that the method is capable of performing under-resolved turbulence simulations with no other stabilization than dissipative numerical fluxes across element boundaries. However, this "no-model" approach becomes questionable with higher order polynomial approximations, when DG comes closer to spectral methods and may lack sufficient dissipation in the interior of the elements. The goal of the present work is to compare the no-model DG method to an LES method, which is augmented by a subgrid-scale model. For this purpose, the dynamic σ-model has to be adapted and implemented for use with the incompressible DG flow solver provided in the HiSPEET library. Using this solver, numerical studies of turbulent flows, such as the decaying Taylor-Green vortex, are to be conducted to assess the accuracy of the σ-model in comparison to the no-model approach depending on the polynomial order used for spatial approximation.

Literatur:

[1] F. Nicoud, H. Baya Toda, O. Cabrit, S. Bose, J. Lee: Using singular values to build a subgrid-scale model for large eddy simulations, Phys. Fluids 23:085106, 2011

Betreuer:	M. Grotteschi MSc.
	PD Dr. J. Stiller
1. Gutachter:	Prof. Dr.-Ing. habil. J. Fröhlich
2. Gutachter:	PD Dr. J. Stiller

Ausgehändigt am:	15.01.2021
Einzureichen am:	15.06.2021

Prof. Dr.-Ing. habil. J. Fröhlich
Betreuender Hochschullehrer

Prof. Dr. techn. M. Tajmar
Studienrichtungsleiter

Kurzfassung

Anpassung und Validierung des σ-Modells für Large-Eddy-Simulationen mit der Diskontinuierlichen Galerkin-Methode

Ziel der vorliegenden Arbeit ist es, die Machbarkeit und Eigenschaften von σ-Modell für Large-Eddy-Simulation in Verbindung mit Diskontinuierlichen Galerkin-Methode zu untersuchen. Dafür sind beide statisches und dynamisches σ-Modell vorgestellt und die werden mittels Taylor-Green Vortex Strömung bei $Re = 1600$ validiert. Für dynamisches Modell, der Vergleich mit No-Modell-Verfahren unter verschiedenen Raumdiskretisierungen, das Verhalten nach h- und P-Verfeinerung, der Effekt des Abbruchspolynomgrads sowie Stabilisierungsmethoden (Clipping und zeitliche Mittelung) sind diskutiert. Für statisches Modell, die Approximationsgenauigkeit und die turbulente Strukturen mit Modellkonstante aus dynamischer Prozedur sind untersucht. Am Ende haben wir begründet, dass die zusätzlichen Kosten akzeptabel sind verglichen mit den Vorteile des σ-Modells.

Abstract

Adaptation and validation of the σ-model for large-eddy simulations with the discontinuous Galerkin method

Aim of the present work is to investigate the feasibility and property of σ-model for large-eddy simulation in combination with the discontinuous Galerkin method. For this purpose, both static and dynamic σ-model are discussed and validated using Taylor-Green Vortex flow with $Re = 1600$. For dynamic model, the comparison with no-model approach under different spatial discretization, the behavior towards h- and P-refinement, the effect of cut-off polynomial order as well as the stabilization techniques (clipping and temporal smoothing) are discussed. For static model, the approximation accuracy as well as the turbulent structures using model constants suggested by dynamic model are investigated. In the end, we argued that the computational cost of σ-model is acceptable in consideration of the advantages it brings.

Contents

Table of Symbols

Latin symbols	Description
C	model constant
c	convective term
$\mathcal{C}_m$	intermediate temporal smoothing expression
$\mathcal{D}$	differential operator
d	dimension
$\det$	determinant
$E(k)$	energy spectrum
E_k	kinetic energy
e	Euler constant
$\boldsymbol{F}$	general function (Chapter 3)
$\boldsymbol{F}$	filter matrix (Chapter 4)
$\boldsymbol{f}$	volume force
$\boldsymbol{G}$	square of $\boldsymbol{g}$
G	filter function (Chapter 2)
$\boldsymbol{g}$	local velocity gradient tensor
g	gradient term
h	mesh size
$\boldsymbol{H}$	numerical flux
$\mathcal{I}$	invariant
j	penalty term
k	wave number
L	exact SGS stress
l	characteristic length scale (Chapter 2)

l	Lagrange basis function (Chapter 3)
M	modelled SGS stress
m	mass matrix term
N	element number
$\boldsymbol{n}$	normal vector
P	polynomial order
P_c	cut-off polynomial order
p	pressure
Q	square of error
q	characteristic velocity scale
Re	Reynolds number
$\boldsymbol{S}$	symmetric part of $\boldsymbol{g}$
S_{ij}	strain rate
T	sub-filter scale viscous stress under test filter
t	time
tr	trace
$\boldsymbol{u}$	velocity
$\boldsymbol{V}, V$	Vandermonde matrix
V	volume (Chapter 5)
$\boldsymbol{v}$	test function
v	viscous term
$\boldsymbol{x}$	displacement
y	displacement to wall

Greek symbols	Description
α	angle
Γ	boundary
Δ	characteristic length
ε	recursive filter parameter
ϵ	dissipation
λ	eigenvalue
μ_v, μ_*	symmetric interior penalty parameters
ν	viscosity
ξ	standard element coordinate
Π	product of a sequence
π	Pi
ρ	density
Σ	sum of a sequence
σ	singular value
$\boldsymbol{\tau}$	viscous stress tensor
τ	sub-grid scale viscous stress
τ_d, τ_j	penalty parameter
ϕ	basis function
$\boldsymbol{\Omega}$	antisymmetric part of $\boldsymbol{g}$
Ω	domain
ω	angular velocity

Indices	Description
e	element
h	discrete solution
i, j, k, l	counter index
La	Lagrange
Le	Legrendre
mod	model
n	time-step
phy	physical
t	turbulent, sub-grid scale

Other symbols	Description
$\langle \cdots \rangle$	spatial average
$\overline{\cdots}$	filtered quantity under grid filter
$\widehat{\cdots}$	filtered quantity under test filter
$\cdot\tilde{\cdot}\cdot$	modal filter
$+$, $-$	neighbor elements
$[\cdots]$	time-step
$\{\{\cdots\}\}$	average operator
$[\![\cdots]\!]$, $[\cdots]$	jump operators

Abbreviation	Description
BDF2	2-step backward differentiation formula
CFL	Courant–Friedrichs–Lewy number
CG	continuous Galerkin
DG	discontinuous Galerkin
DNS	direct numerical simulation
DoF	degree of freedom
DPT	discrete polynomial transformation
FEM	finite element method
FVM	finite volume method
GLL	Gauss-Lobatto-Legendre
HiSPEET	high-performance spectral element library
ILES	implicit large-eddy simulation
LES	large-eddy simulation
LF	Lax-Friedrichs
LLF	local Lax-Friedrichs
NSE	Navier-Stokes equations
SGS	sub-grid scale
SIP	symmetric interior penalty
TGV	Taylor-Green Vortex
WALE	wall adapting local eddy

1 Introduction

The high-order methods of computational fluid dynamics based on the finite volume approach are nowadays an important research area for fluid simulation techniques due to their high accuracy and high fidelity. Among those methods, the discontinuous Galerkin (DG) method is one of the most prospective candidates for its flexibility and high parallelism which is particularly attractive for high-performance computing. Despite of the development of more powerful computer and improved efficiency of high-order flow solvers, the direct numerical simulation (DNS) of turbulent flow problems still seems to be too expensive and sometimes infeasible. Therefore, the widely used large-eddy simulation (LES) by which only the large-scale vortices are resolved is naturally introduced to DG methods.

Up to now, most of the studies for LES based on DG method employ no-model approach (or Implicit LES, ILES). The basic idea of no-model approach is to use the dissipation effect of DG discretization scheme, such as the explicit treatment of convection term to serve as the sub-grid scale (SGS) dissipation in traditional LES methods. Among all the studies, Beck et al. [1] have compared the dissipation effect of Lax-Friedrichs (LF) flux and Roe's flux for Taylor-Green Vortex (TGV) flow under $Re = 800, 1600, 3000$ respectively. Gassner et al. [2] have investigated the accuracy of under-resolved turbulent simulations using different stabilization techniques (filtering and overintegration) using the same simulation configuration. Fehn et al. [3] presents a comparative study of L2- and H(div)-based DG approaches, in which the effect of numerical dissipation is investigated in detail under different spatial discretization techniques. However, the consistency no-model approach becomes questionable when the polynomial order gets higher, as the numerical dissipation caused by numerical flux reduces significantly and the approximation may lack of SGS dissipation.

As for the attempts with explicit modeling of SGS stress, most of the work concern with the Smagorinsky model. Brazell et al. [4] have performed static and dynamic Smagorinsky models for TGV flow under $Re = 1600$ with DG method. Chapelier et al. [5] have developed a multiscale LES model for DG method which is validated using TGV flow and Smagorinsky model as example. In their work, the high accuracy and consistency of explicit SGS model are emphasized particularly for high Reynolds-number. For dynamic SGS models, Blackbrun et al. [6] suggested several element-level spectral filtering techniques based on the modal and nodal basis transformations and applied the dynamic Smagorinsky model to turbulent flow simulation.

Despite of the wide range applications of classical Smagorinsky model, the attempt of developing further explicit SGS models in order to overcome the shortage of Smagorinsky model has never been stopped. For example, the wall adapting local eddy (WALE) viscosity and Vreman's model are proposed to obtain better approximation of near-wall areas and turbulent shear flows. Recently, Nicoud et al. [7] have suggested a new SGS model which is based on the singular values of the

velocity gradient tensor $\boldsymbol{g} = (g_{ij}) = (\partial u_i / \partial x_j)$. The so-called σ-model shows its superiority for improved accuracy in near-wall region, two-dimensional flow and isotropic turbulence.

So far as we know, there is still very little references of σ-model combined with DG method. In the present work, we aim to adapt the σ-model to the high-order turbulent flow solver. Based on the high-performance spectral element library (HiSPEET) developed by Professur für Strömungsmechanik, we implement the static and dynamic σ-model for DG approach of convection-diffusion problem and try to analyze the property and accuracy of the model. For validation, the three-dimensional TGV flow with $Re = 1600$ is employed as a prototype of various phenomena of turbulent flows. At the end, the effect of σ-model will be evaluated from the performance perspective and some other stabilization techniques will also be analyzed.

2 Large-Eddy Simulation

2.1 The Navier-Stokes equations

For any kind of flow simulations including the LES, the starting point should be the Navier-Stokes equations (NSE), which govern the fluid motion. Here we consider the incompressible, constant-density form of Navier-Stokes equations, which include the mass and impulse conservation in terms of the three-dimensional time-varying velocity vector $\boldsymbol{u}(\boldsymbol{x}, t)$

$$\nabla \cdot \boldsymbol{u} = 0 \quad , \tag{2.1}$$

$$\partial_t \boldsymbol{u} + \nabla \cdot \boldsymbol{u}\boldsymbol{u} + \nabla p = \nabla \cdot \boldsymbol{\tau} + \boldsymbol{f} \tag{2.2}$$

in a simply connected domain $\Omega \in \mathbb{R}^3$. Here p represents the pressure while $\boldsymbol{\tau}$ is the viscous stress tensor. For the problem with variable viscosity ν, the viscous term can be written as

$$\nabla \cdot \boldsymbol{\tau} = \nabla \cdot \nu \left[\nabla \boldsymbol{u} + (\nabla \boldsymbol{u})^{\mathrm{T}}\right] \quad . \tag{2.3}$$

2.2 Basic idea

The execution of a DNS for turbulent flows with many small-scale turbulent structures can be very expensive, where high grid resolution and small time-step size are required. In these scenarios the LES which resolves only large-scale vortices can significantly reduce the computational cost, since a coarser grid and larger time-step size can be used. However, the large-scale vortices can not behave correctly when the fine-scale motions are completely ignored. In order to involve the effect of the under-resolved (or subgrid-scale) fluid motions on the coarse grid, the SGS models are introduced. From this point of view, the LES plays a role like a ”poor man’s DNS”. [8] Generally, the SGS motions are modeled as an additional viscous effect (the eddy viscosity ν_t) applied to well resolved large eddies, which makes the total viscosity of fluid vary in space and time.

2.3 Filtering

For clarity and simplicity of the derivation, the tensors that appear in NSE (such as $\boldsymbol{u}$, $\boldsymbol{\tau}$) are written in component-wise till the end of this chapter. We also assume that the volume force term is ignorable in our illustration, e.g. $\boldsymbol{f} \equiv \boldsymbol{0}$.

The filtered velocity component in velocity $\boldsymbol{u}$, denoted by $\overline{u}_i$, is defined by Leonard as

$$\overline{u}_i(x) = \int_{-\infty}^{+\infty} G\left(x - x'\right) u\left(x'\right) dx' \quad , \tag{2.4}$$

where G is the filter function with $\int G(x)dx = 1$ and its filter width $\bar{\Delta}$. The common filter settings are for example Gaussian filter and box filter. Another appropriate thought is to transfer filter functions in Fourier space so that the modal filter can be applied to variables in NSE:

$$\tilde{u}_i(\omega) = \int_{\Omega} u_i(x) e^{-i\omega x} dx \quad , \tag{2.5a}$$

$$\widetilde{\overline{u}}_i(\omega) = \tilde{G}(\omega)\tilde{u}_i(\omega) \quad . \tag{2.5b}$$

With the digital filters above, the variables in NSE (Equation 2.1, 2.2) can be filtered on a LES grid. The NSE being applied with filter operation read

$$\frac{\partial \overline{u}_i}{\partial x_i} = 0 \quad , \tag{2.6}$$

$$\frac{\partial \overline{u}_i}{\partial t} + \frac{\partial \left(\overline{u_i u_j}\right)}{\partial x_j} + \frac{\partial \overline{p}}{\partial x_i} = \frac{\partial \left(\nu 2 \overline{S}_{ij}\right)}{\partial x_j} \quad . \tag{2.7}$$

Using the identity $\overline{u_i u_j} = \tau_{ij}^{\mathrm{SGS}} + \overline{u}_i \overline{u}_j$, where the term τ_{ij}^{SGS} represents the influence of unresolved fluid motions on resolved ones, the Equation 2.7 can be reformulated as

$$\frac{\partial \overline{u}_i}{\partial t} + \frac{\partial \left(\overline{u}_i \overline{u}_j\right)}{\partial x_j} + \frac{\partial \overline{p}}{\partial x_i} = \frac{\partial \left(\nu 2 \overline{S}_{ij}\right)}{\partial x_j} - \frac{\partial \tau_{ij}^{\mathrm{SGS}}}{\partial x_j} \quad . \tag{2.8}$$

2.4 Explicit LES modeling

2.4.1 Sub-grid scale model

The SGS model is a particular feature of LES which aims to model the sub-grid scale fluid motions, e.g. the SGS stress τ_{ij}^{SGS}. Following the idea that the effect of unresolved turbulent motions can be regarded as an additional viscosity on the LES-level grid, it is intuitive to formulate the SGS stress like the viscous term in Equation 2.8, which means

$$\tau_{ij}^{\mathrm{SGS}} = \nu_t 2 \overline{S}_{ij} \quad , \tag{2.9}$$

where the eddy viscosity ν_t varies in space and time. From the dimension analysis, the expression of ν_t should be

$$\nu_t \propto l q_{\mathrm{SGS}} \quad , \tag{2.10}$$

where l is the length scale of unresolved motions, usually the filter size Δ, and q_{SGS} the velocity scale. Furthermore, the velocity scale q_{SGS} can be expressed as the product of the length scale l and a differential operator $\mathcal{D}_m$ which acts on the resolved velocity field $\overline{u}$ and is associated with the model. In this way, the eddy viscosity ν_t reads

$$\nu_t = (C_m \Delta)^2 \mathcal{D}_m \quad , \tag{2.11}$$

where $l = C_m \Delta$ is assumed. Here the model constant C_m is predetermined and should be irrelevant to fluid situations, and the differential operator $\mathcal{D}_m$ varies in space and time associated with local flow situation.

2.4.2 The characteristic length Δ

Besides the model constant C_m and the differential operator $\mathcal{D}_m$, the characteristic length (or cut-off length, when we use a sharp modal filter) Δ, which provides the information about the width of filters, also plays an important role by the SGS viscosity model [9]. Despite of the fact that the choice of filtering parameters is irrelevant to the LES-grid width, however, the grid mesh size h is always chosen as large as the characteristic length Δ, such that the maximum computational efficiency is achieved. In this way, $\Delta = h$ is set for LES simulation and the mesh size h is thus called the "grid filter".

When the applied grid is anisotrop, e.g. $\Delta_x \neq \Delta_y \neq \Delta_z$, Δ must be determined according to the actual conditions. For example, Deardoff [10] used

$$h = (\Delta_x \Delta_y \Delta_z)^{1/3} \tag{2.12}$$

while in [11] the geometric average is used

$$h = \frac{1}{3}\sqrt{\Delta_x^2 + \Delta_y^2 + \Delta_z^2} \quad . \tag{2.13}$$

Inspired from the consideration that the vortex movement will be affected once it can not be resolved in a single dimension of three, one can also use the maximal mesh size dimension

$$h = \max(\Delta_x, \Delta_y, \Delta_z) \tag{2.14}$$

as a characteristic length [12].

2.5 No-model approach

In the last section, we have introduced the possibility to use an explicitly defined SGS model as the filter. In fact, the discretization schemes itself can also serve as a LES filter. For example, the numerical errors can cause velocity jumps at the element boundary results in the additional dissipative effect by some explicit treatments of convective term, and this dissipative effect undertakes the role of SGS stress. Since that the SGS stress tensor is contained within the numerical scheme, an explicit computation is no more needed. Therefore, this method is also called implicit large-eddy simulation (ILES). We may notice that the ILES method relies more on numerical treatments, such as choice of numerical flux and spatial discretization, rather than the physical essence of turbulent flow development. Despite of that, the ILES method is still widely adopted and deeply researched, particularly for the under-resolved turbulent flow with high-order methods.

3 Discontinuous Galerkin Method

3.1 Basic idea

Discontinuous Galerkin (DG) methods belong to the class of finite element methods (FEM). They combine features in FEM (weak formulation, finite dimensional solution and test function spaces) and FVM (numerical fluxes, nonlinear limiters) [13]. The main feature of DG methods, particularly compared with continuous Galerkin (CG) methods is that, the piecewise polynomial bases are allowed to be completely discontinuous across element interfaces. Since the values can be indeterminate at element interfaces regarding to jumped results from different elements at the same boundary, the concept of numerical flux which comes from FVM is introduced into DG schemes. To illustrate this, we take a simple partial equation with time and space derivatives

$$\frac{\partial \boldsymbol{u}}{\partial t} + \nabla \cdot \boldsymbol{F}(\boldsymbol{u}) = 0 \tag{3.1}$$

in $\Omega \times [0, T], \Omega \in \mathbb{R}^d$ as example. Assuming that the computational domain Ω^h is spatially divided into N parts (or elements)

$$\Omega^h = \bigcup_{e=1}^{N} \Omega^e \quad , \tag{3.2}$$

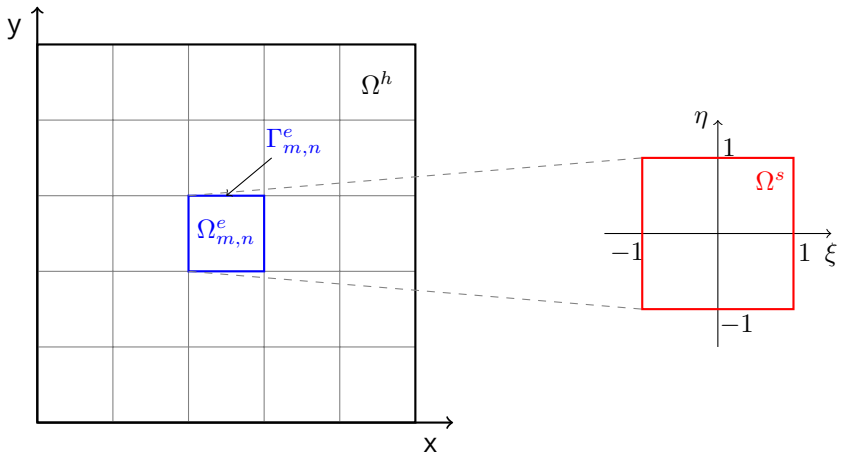

Figure 3.1: 2D sketch of computational domain Ω^h, element Ω^e, its boundary Γ^e and its mapping Ω^s in standard element space.

and Γ^e denotes the boundary of element. The space of test functions $\boldsymbol{v}_h(\boldsymbol{x}, t) \in \mathcal{V}_h^v$ is defined as

$$\mathcal{V}_h^v = \{\boldsymbol{v}_h \in L^2(\Omega) : \boldsymbol{v}_h^e \in \mathcal{P}^d \quad \forall \Omega^e \in \Omega^h\} \quad . \tag{3.3}$$

The semi-discrete DG method to solve Equation 3.1 is defined as follows: find the unique solution $\boldsymbol{u}_h(t) \in \mathcal{V}_h^v$ that satisfies following equation for all test functions and all elements:

$$\int_{\Omega^e} \frac{\partial \boldsymbol{u}_h}{\partial t} \cdot \boldsymbol{v}_h d\Omega + \int_{\Omega^e} (\nabla \cdot \boldsymbol{F}(\boldsymbol{u}_h)) \cdot \boldsymbol{v}_h d\Omega = 0 \quad . \tag{3.4}$$

Due to the time-irrelevant test functions $\boldsymbol{v}_h$ and using the integration by parts for the second term, Equation 3.4 becomes

$$\frac{\partial}{\partial t} \int_{\Omega^e} \boldsymbol{u}_h \cdot \boldsymbol{v}_h d\Omega - \int_{\Omega^e} \boldsymbol{F}(\boldsymbol{u}_h) : \nabla \boldsymbol{v}_h d\Omega + \int_{\Gamma^e} \boldsymbol{v}_h : \boldsymbol{F}(\boldsymbol{u}_h) d\Gamma = 0 \quad . \tag{3.5}$$

Adding up all the element integrals in Equation 3.5 provides the global weak form for Ω^h

$$\frac{\partial}{\partial t} \int_{\Omega^h} \boldsymbol{u}_h \cdot \boldsymbol{v}_h d\Omega - \int_{\Omega^h} \boldsymbol{F}(\boldsymbol{u}_h) : \nabla \boldsymbol{v}_h d\Omega + \sum_{\Gamma^e} \int_{\Gamma^e} \boldsymbol{v}_h : \boldsymbol{F}(\boldsymbol{u}_h) d\Gamma = 0 \quad . \tag{3.6}$$

Note that $\boldsymbol{F}(\boldsymbol{u})$ is ambiguous at the element boundary since the neighbor of the element provides a different value for the same variable, the numerical flux function $\boldsymbol{H}$ is introduced here to unify the boundary value, for example at the boundary $e + 1/2$,

$$\boldsymbol{H}^{e+1/2} = \boldsymbol{F}(\boldsymbol{u}_h)^{e+1/2} := \boldsymbol{H}(\boldsymbol{u}_h^e(\boldsymbol{x}^{e+1/2}), \boldsymbol{u}_h^{e+1}(\boldsymbol{x}^{e+1/2})) \quad . \tag{3.7}$$

3.2 Basis function

The weak DG formulation uses a series of polynomials as its basis functions, which means that both $\boldsymbol{u}_h$ and $\boldsymbol{v}_h$ inside the element can be written as sum of a set of polynomials

$$\boldsymbol{u}_h^e(\boldsymbol{x}) = \sum_{i=0}^{N} \hat{u}_i^e \boldsymbol{\phi}_i^e(\boldsymbol{x}) \tag{3.8}$$

and

$$\boldsymbol{v}_h^e(\boldsymbol{x}) = \sum_{i=0}^{N} \hat{v}_i^e \boldsymbol{\phi}_i^e(\boldsymbol{x}) \quad . \tag{3.9}$$

Generally, two kinds of polynomials are employed as basis functions $\boldsymbol{\phi}_i^e(\boldsymbol{x})$, namely the modal (such as Legendre) polynomials and nodal (such as Lagrange) polynomials. We now focus on one-dimensional polynomials with order $[0, P] \in \mathbb{N}$ in the standard element $\Omega^s \in [-1, 1]$, which can be easily extended to three-dimensional case by means of tensor product.

The Legendre polynomials are a subclass of Jacobi polynomials, who own a hierarchical structure. The expansion of polynomial subset is possible by simply adding the higher-order polynomials without modifying present ones. The Legendre polynomials can be defined by various methods. A

general definition using recursive formula reads

$$\begin{aligned} P_0 &= 1 && ; \\ P_1 &= \xi && ; \\ P_{k+1} &= \frac{(2k+1)\xi P_k - kP_{k-1}}{k+1} && . \end{aligned} \tag{3.10}$$

As we just mentioned, the Legendre basis belongs to the category of "modal basis", whose basis functions are arranged from low to high orders. This makes the Legendre basis a natural candidate of modal filtering, particularly considering its association to Gauss-quadrature compared with Chebyshev polynomials. [6]

On the other hand, the Lagrange polynomials are used as "nodal" basis for spectral methods, and the hierarchical property is no more reserved. However, it is still orthogonal up to degree $2P$ and brings a direct access to the Gauss-quadrature when adopting Gauss-Lobatto-Legendre (GLL) quadrature points. Given the quadrature points $\{\xi_i\}_{i=0}^{P}$, the Lagrange basis can be generated using the formula

$$l_i(\xi) = \prod_{j=0, j\neq i}^{P} \frac{\xi - \xi_j}{\xi_i - \xi_j}, \quad 0 \leq i \leq P \quad . \tag{3.11}$$

A comparison of Legendre and Lagrange basis for polynomial order $P = 5$ is shown in Figure 3.2.

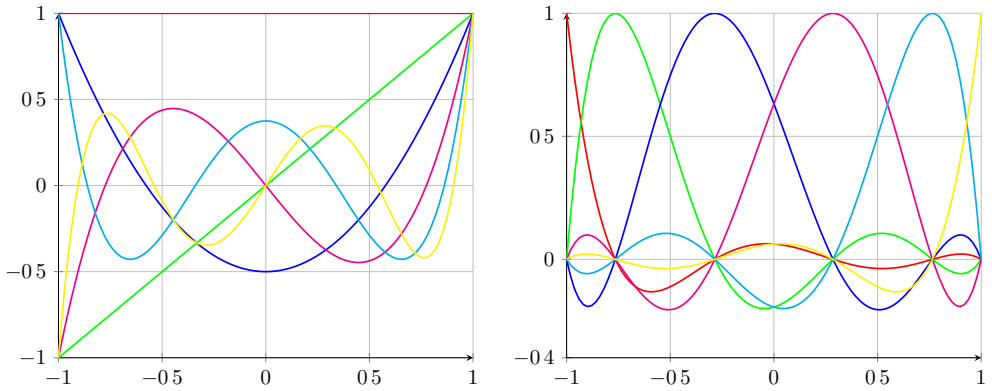

Figure 3.2: A comparison of (a) Legendre (b) Lagrange polynomials (GLL points) for polynomial order $P = 5$.

The Legendre polynomials P_j can be decomposed into Lagrange polynomials

$$P_j(\xi) = \sum_{i=0}^{p} V_{ij} l_i(\xi) \quad , \tag{3.12}$$

where the elements of Vandermonde matrix $\boldsymbol{V}$

$$V_{ij} = \sum_{i=0}^{p} P_j(\xi_i) l_i(\xi) \tag{3.13}$$

serves as linkage between Legendre and Lagrange basis systems. Therefore, an approximated function $u(\xi)$ can be expressed in both bases equivalently

$$u(\xi) = \sum_{j=0}^{P} u_j^{\mathrm{Le}} P_j(\xi) = \sum_{i=0}^{P} u_i^{\mathrm{La}} l_i(\xi) \quad . \tag{3.14}$$

With definition of vector of coefficient $\underline{u}^{\mathrm{Le}} = \{u_i^{\mathrm{Le}}\}_{i=0}^{p}$ and $\underline{u}^{\mathrm{La}} = \{u^{\mathrm{La}} i\}_{i=0}^{p}$ for Legendre and Lagrange basis respectively, the transformations between Legendre and Lagrange coefficients via Vandermonde matrix read

$$\underline{u}^{\mathrm{La}} = \boldsymbol{V} \underline{u}^{\mathrm{Le}} \quad , \tag{3.15a}$$

$$\underline{u}^{\mathrm{Le}} = \boldsymbol{V}^{-1} \underline{u}^{\mathrm{La}} \quad . \tag{3.15b}$$

3.3 DG building blocks

3.3.1 Preliminaries

For spatial discretization and time integration of weak Navier-Stokes equations, we use the High-performance SPEctral Element Techniques library (HiSPEET) developed by Professur für Strömungsmechanik at TU Dresden. Before getting into DG blocks to discretize the Navier-Stokes Equations 2.1 and 2.2, we must define the standard average and jump operators to deal with the discontinuity at element boundary.

For every interior face Γ_I^e there exists two adjoining elements, denoted by Ω^- and Ω^+ with their normal vectors $\boldsymbol{n}^-$ and $\boldsymbol{n}^+$ respectively. For a element-wise continuous function ϕ, the average operator $\{\{\boldsymbol{\phi}\}\}$ and jump operators $[\![\boldsymbol{\phi}]\!]$ (for scalars) and $[\boldsymbol{\phi}]$ (for vectors and tensors) are defined as

$$\{\{\boldsymbol{\phi}\}\} = \frac{1}{2}(\boldsymbol{\phi}^- + \boldsymbol{\phi}^+) \quad , \tag{3.16}$$

$$[\![\boldsymbol{\phi}]\!] = \boldsymbol{n}^- \boldsymbol{\phi}^- + \boldsymbol{n}^+ \boldsymbol{\phi}^+ \quad , \tag{3.17}$$

$$[\boldsymbol{\phi}] = \boldsymbol{n}^- \cdot \boldsymbol{\phi}^- + \boldsymbol{n}^+ \cdot \boldsymbol{\phi}^+ \quad . \tag{3.18}$$

Note that the jump operation for a scalar $[\![\phi]\!]$ results in a vector, and $[\boldsymbol{\phi}]$ for a vector results in a

scalar follows the inner product, which means that for a vector function, only the normal component (to the element face) is considered in the jump operator $[\,]$.

3.3.2 Weak formulated terms

In this section, we introduce the weak formulation of discrete counterparts of various terms in a classical transport equation like Equation 3.1, including the divergence term, mass matrix term, convective term, diffusive term and gradient term. The divergence term d_h^e, mass matrix term m_h^e and gradient term g_h^e with test function $\boldsymbol{v}_h$ or v_h reads

$$d_h^e(\boldsymbol{u}_h, v_h) = \int_{\Omega^e} \nabla v_h \cdot \boldsymbol{u}_h \mathrm{d}\Omega + \int_{\Gamma^e} [\![v_h]\!] \cdot \{\{\boldsymbol{u}_h\}\} \mathrm{d}\Gamma \quad , \tag{3.19}$$

$$m_h^e(\boldsymbol{u}_h, \boldsymbol{v}_h) = \int_{\Omega^e} \boldsymbol{v}_h \cdot \boldsymbol{u}_h \mathrm{d}\Omega \quad , \tag{3.20}$$

$$g_h^e(p_h, \boldsymbol{v}_h) = \int_{\Omega^e} \boldsymbol{v}_h \cdot \nabla p_h \mathrm{d}\Omega = -\int_{\Omega^e} (\nabla \cdot \boldsymbol{v}_h) p_h \mathrm{d}\Omega + \int_{\Gamma^e} [\boldsymbol{v}_h] \{\{p_h\}\} \mathrm{d}\Gamma \quad . \tag{3.21}$$

For convection term c_h^e, the local Lax-Friedrichs (LLF) flux is applied

$$c_h^e(\boldsymbol{u}_h, \boldsymbol{v}_h) = \int_{\Omega_h} \boldsymbol{v}_h \cdot (\nabla \cdot \boldsymbol{u}_h) \boldsymbol{u}_h) \mathrm{d}\Omega = \int_{\Omega^h} \nabla \boldsymbol{v}_h : \boldsymbol{u_h} \boldsymbol{u_h} d\Omega - \int_{\Gamma^h} [\![\boldsymbol{v}_h]\!] : (\{\{\boldsymbol{u}_h \boldsymbol{u}_h\}\} + \hat{u}_n [\![\boldsymbol{u}_h]\!]) \mathrm{d}\Gamma \tag{3.22}$$

with $\hat{u}_n = \max(|\boldsymbol{n} \cdot \boldsymbol{u}_h^-|, |\boldsymbol{n} \cdot \boldsymbol{u}_h^+|)$. We denote that the additional term $\hat{u}_n [\![\boldsymbol{u}_h]\!]$ with velocity jump shows an artificial dissipative behavior, which is widely used as the additional dissipation for no-model approaches. However, we also see that the dissipative effect of LLF flux relied strongly on the velocity jumps at the element boundary, which indicates that this method may depend more on discretization schemes rather than physical essence.

The viscous terms v_h^e with variable viscosity ν_h are discretized using the symmetric interior penalty (SIP) method, which gives

$$\begin{aligned} v_h^e(\nu_h, \boldsymbol{u}_h, \boldsymbol{v}_h) &= \int_{\Omega_h} \boldsymbol{v}_h \cdot (\nabla \cdot \nu_h \nabla \boldsymbol{u}_h) \mathrm{d}\Omega \\ &= -\int_{\Omega_h} \nu_h \nabla \boldsymbol{v}_h : \nabla \boldsymbol{u}_h \mathrm{d}\Omega \\ &\quad + \int_{\Gamma_h} [\![\boldsymbol{v}_h]\!] : \{\{\nu_h \nabla \boldsymbol{u}_h\}\} + \{\{\nu_h \nabla \boldsymbol{v}_h\}\} : [\![\boldsymbol{u}_h]\!] \mathrm{d}\Gamma \\ &\quad - \int_{\Gamma_h} \mu_v \hat{\nu} [\![\boldsymbol{v}_h]\!] : [\![\boldsymbol{u}_h]\!] \mathrm{d}\Gamma \end{aligned} \tag{3.23}$$

where $\mu_v = \mu_\star(p_v)$ and $\hat{\nu} = \max(\nu_h^-, \nu_h^+)$.

3.3.3 Divergence and mass-flux stabilization

The divergence and mass-flux penalty term is employed as a post-processing step to stabilize the pressure projection operator for incompressible flow solver. The penalty term reads

$$j_h^e(\boldsymbol{u}_h, \boldsymbol{v}_h) = \int_{\Omega^e} \tau_d (\nabla \cdot \boldsymbol{v}_h)(\nabla \cdot \boldsymbol{u}_h) \mathrm{d}\Omega + \int_{\Gamma^e} \tau_j [\boldsymbol{v}_h][\boldsymbol{u}_h] \mathrm{d}\Gamma \quad , \tag{3.24}$$

where τ_d and τ_j are penalty coefficients scaled with velocity. It is obvious that the first term on the right-hand side penalizes the velocity divergence inside the element while the second penalizes the discontinuity at the element boundary. This term disappears automatically for the vector field, which is continuous at element boundary and divergence-free inside the element. For more details about the penalty term, readers may refer to the work of Stiller [14].

4 Adaptation of σ-Model with Discontinuous Galerkin Method

4.1 Discretization scheme

4.1.1 Spatial discretization

In this section, we perform the weak DG-formulation applied to the filtered Navier-Stokes equations on the LES grid. The LES formulation in terms of filtered three-dimensional velocity $\overline{\boldsymbol{u}} = [\overline{u}_1\ \overline{u}_2\ \overline{u}_3]^T$ reads

$$\nabla \cdot \overline{\boldsymbol{u}} = 0 \quad , \tag{4.1a}$$

$$\partial_t \overline{\boldsymbol{u}} + \nabla \cdot \overline{\boldsymbol{u}}\overline{\boldsymbol{u}} + \nabla \bar{p} = \nabla \cdot \nu(\nabla \overline{\boldsymbol{u}} + \nabla \overline{\boldsymbol{u}}^T) \quad . \tag{4.1b}$$

It is worth noting that in Equation 4.1b, the variable viscosity $\nu(\boldsymbol{x}, t) = \nu_{\mathrm{phy}} + \nu_{\mathrm{SGS}}(\boldsymbol{x}, t)$ includes both constant physical viscosity as well as SGS viscosity, where the SGS stress is modeled explicitly. Besides, the volume force is not considered in our case. With the help of the matrix terms defined in Section 3.3.2, the weak formulation of Equation 4.1 reads

$$d_h^e(\boldsymbol{u}_h, v_h) = 0 \quad , \tag{4.2a}$$

$$m_h^e\left(\frac{\partial \boldsymbol{u}_h}{\partial t}, \boldsymbol{v}_h\right) + c_h^e\left(\boldsymbol{u}_h, \boldsymbol{v}_h\right) + g_h^e\left(p_h, \boldsymbol{v}_h\right) = v_h^e\left(\nu_h, \boldsymbol{u}_h, \boldsymbol{v}_h\right) + v_h^e\left(\nu_h, \boldsymbol{u}_h^T, \boldsymbol{v}_h\right) \quad , \tag{4.2b}$$

where the velocity vector $\boldsymbol{u}_h$, test functions $\boldsymbol{v}_h, v_h$ and other functions p_h, ν_h are approximate values on the grid points. The local Lax-Friedrich flux is employed for the convective term c_h^e, while the symmetric interior penalty (SIP) method is used to discretize the diffusive term v_h^e. To stabilize the DG method, the overintegration of convective term with $3/2P + 1$ quadrature points and the mass-flux and divergence penalty terms are applied. For detailed information, readers may refer to the work of Stiller [14]. For time integration, the BDF2 method with dual-splitting scheme based on the projection method is employed.

4.1.2 Time-step size and CFL condition

For the sake of numerical stability, the time-step size Δt must be reduced regarding mesh refinement. To be specific, for convection-dominated cases, the critical Courant-Friedrichs-Lewy (CFL) number

should not be exceeded

$$\mathrm{CFL}^* = \frac{\Delta t^* ||\boldsymbol{u}||_{\max}}{\delta} \quad , \tag{4.3}$$

where the length scale characterizing δ is generally expressed as a function of refinement parameters h and P for high-order methods. Fehn et al. [15] reported that for $\delta_1 = h/P^{1.5}$, $\mathrm{CFL}^* = 0.18..0.20$ is valid for a wide range of discretization parameters. In order to minimize the influence of time integration errors, we adopt

$$\mathrm{CFL} = \frac{\Delta t ||\boldsymbol{u}||_{\max}}{h/P^{1.5}} = 0.1 \tag{4.4}$$

for all the simulations.

4.2 The σ-model

An explicit SGS model proposed by Nicoud et al. [7] uses singular values for evaluation of eddy viscosity. The resulted SGS model and proposed differential operator read

$$\nu_t = (C_\sigma \Delta)^2 \mathcal{D}_\sigma \quad , \tag{4.5}$$

$$\mathcal{D}_\sigma = \frac{\sigma_3(\sigma_1 - \sigma_2)(\sigma_2 - \sigma_3)}{\sigma_1^2} \quad , \tag{4.6}$$

where $\sigma_1 > \sigma_2 > \sigma_3 \geq 0$ are three singular values of filtered local velocity gradient tensor $\bar{\mathbf{g}} = (\bar{g}_{ij}) = (\partial \bar{u}_i / \partial x_j)$ ordered from large to small.

Some desirable properties of an explicit SGS viscosity model are listed in Table 4.1. Note that for explicit SGS models, these properties should be met by differential operators $\mathcal{D}_m$ of each model. Obviously, the σ-model owns more desirable properties than other candidates. Firstly, due to the organization of singular values in Equation 4.6, a locally defined positive $\mathcal{D}_\sigma$ is always ensured, which only relies on the local velocity gradient tensor $\bar{\mathbf{g}}$. In this way, a positive SGS viscosity is also ensured to avoid numerical stability issues (**Property P0**). Secondly, the asymptotic analysis shows that in the near-wall region, the singular values own the properties

$$\begin{aligned} \sigma_1 &= O(y^0) \\ \sigma_2 &= O(y^1) \\ \sigma_3 &= O(y^2) \quad , \end{aligned} \tag{4.7}$$

which ensure an ideal near-wall behavior of $\mathcal{D}_\sigma = O(y^3)$ (**Property P1**). Furthermore, the smallest singular value of velocity gradient tensor σ_3 becomes zero if one row or column of $\bar{\mathbf{g}}$ is zero, which leads to $\mathcal{D}_\sigma = 0$ corresponding to the two-component or two-dimensional case (**Property P2**). We denote here that the concept of two-component or two-dimensional turbulent flows do exists

and sometimes worth researching in detail. However, the mechanism and behavior (for example, vortex stretching) of a two-dimensional flow is totally different with a three-dimensional case. Given this, the effect of two-dimensional behaviors should not play a role in 3D simulations. Finally, for an axisymmetric or isotropic configuration, $\mathcal{D}_\sigma$ also turns to zero since $\sigma_1 = \sigma_2$ or $\sigma_2 = \sigma_3$ and $\sigma_1 = \sigma_2 = \sigma_3$, for these cases respectively, through which the **Property P3** is met.

Table 4.1: Desirable properties for an explicit SGS model [7]

P0	a positive quantity which involves locally defined velocity gradients
P1	cubic behavior near solid boundaries
P2	zero for any two-component or two-dimensional flows
P3	zero for axisymmetric or isotropic expansion/ contraction

Last but not least, the computational cost of σ-model is reported to be acceptable compared with Smagorinsky model. Particularly, for three-dimensional square matrix $\bar{\mathbf{g}}$, the calculation of singular values can be highly customized, which reduces the computation time further. There exist alternative ways to calculate the singular value of local velocity gradient tensor, see Appendix A.1.

4.3 The characteristic length Δ

As discussed in Section 2.4.2, the characteristic length Δ is usually selected as the grid width h, where we see various definitions of h for isotropic elements ($\Delta_x \neq \Delta_y \neq \Delta_z$). For classic finite volume method, the discretization is entirely decided by the mesh size h. For high-order methods on the other side, the spatial discretization relies on both the mesh size h and the polynomial order P. Therefore, the definition of Δ is more flexible but more tricky. Up to now, we have seen several suggestions on definition of Δ regarding the DG methods. Van Der Bos et al. [16] propose

$$\Delta = \frac{C_s^*}{0.17} h \tag{4.8}$$

for Smagorinsky model, where C_s^* is an optional value to adapt to the model constant. Marek et al. [17] use

$$\Delta = \frac{h}{P+1} \tag{4.9}$$

with an emphasis that the definition of Δ reduces to finite volume method by choosing $P = 0$. In the work of Brazell et al. [4], the characteristic length is defined as

$$\Delta = \frac{h}{2(P+1)} \quad , \tag{4.10}$$

but no clear reason of this definition is stated. Chapelier et al. [5] calibrated the Smagorinsky model constant using the DG transfer function and find that the relation

$$\Delta \sim \frac{h}{P} \tag{4.11}$$

is accurate enough for Smagorinsky model under a wide range of polynomial orders. Among these works, we find that the recommended model constant is generally no more suitable for Δ as a function of h and P under DG methods, thus either the model constant or the characteristic length needs to be calibrated.

In the present work, we use

$$\Delta = \frac{h}{P} \tag{4.12}$$

as practical definition of Δ, where $h = (\Delta_x \Delta_y \Delta_z)^{1/3}$. Inspiration of this definition is to take the length of subinterval inside the element as the characteristic length, where the size of element h is divided into P subintervals. Due to the absence of a linear coefficient before h/P, the model constant C suggested for simple FDM or FVM must be reevaluated for DG methods.

4.4 Dynamic σ-model

4.4.1 The dynamic procedure

Despite of the wide application of static SGS model, one notice that a predetermined model constant is sometimes unsuitable for certain cases and brings negative effects. For example, for the on LES-grid well resolved laminar flow, the present of model constant and followed ν_t are apparently too dissipative and unnecessary. In those cases, we hope that the model constant can automatically reduce or even vanish to avoid the ”disservice” on the numerics. To be generic, the space and time varying model constant is in the most of situations more desirable than the fixed constant.

One of the solutions, called the dynamic procedure, is developed by Germano [18] to estimate a dynamically varying model constant from the resolved flow motions. The fundamental of estimation is the self-similarity of turbulent structures in the inertial range of energy spectrum, which means that the model constant should remain the same while modeling the SGS stress between resolved and under-resolved scales as well as two differently resolved scales. Therefore, besides the inherent grid filter of LES-scale, a coarser filter (called test filter) is employed to give the information on the other resolved scale. The test filter scale is denoted by $\widehat{\Delta}$, which is usually set to be $\widehat{\Delta} = 2\overline{\Delta}$ for convenience. With the relation $\tau_{ij} = \overline{u_i u_j} - \overline{u_i}\,\overline{u_j}$ and $\tau_{ij}^{\mathrm{mod}} = -2\nu_t \overline{S_{ij}}$, the expression of SGS stress

tensors under both filter scales $\overline{\Delta}$ and $\widehat{\Delta}$ can be formulated as

$$\tau_{ij} = \overline{u_i u_j} - \overline{u_i}\,\overline{u_j} \approx \tau_{ij}^{\mathrm{mod}}(C, \overline{\Delta}, \overline{u}) \quad , \tag{4.13a}$$

$$T_{ij} = \widehat{\overline{u_i u_j}} - \widehat{\overline{u_i}}\,\widehat{\overline{u_j}} \approx \tau_{ij}^{\mathrm{mod}}(C, \widehat{\Delta}, \widehat{\overline{u}}) \quad , \tag{4.13b}$$

where the term T_{ij} denotes the SGS stress tensor on test scale. The term in $\widehat{\overline{u_i u_j}}$ in T_{ij} can be substituted with the expression of τ_{ij}, namely

$$T_{ij} = \widehat{\tau_{ij}} + \widehat{\overline{u_i}\,\overline{u_j}} - \widehat{\overline{u_i}}\,\widehat{\overline{u_j}} = \widehat{\tau_{ij}} + L_{ij} \quad , \tag{4.14}$$

where

$$L_{ij} = T_{ij} - \widehat{\tau_{ij}} = \widehat{\overline{u_i}\,\overline{u_j}} - \widehat{\overline{u_i}}\,\widehat{\overline{u_j}} \tag{4.15}$$

is in fact the difference of SGS stress tensors between two filter scales. Meanwhile, this difference given by a certain SGS model L_{ij}^{mod} can be expressed as:

$$\begin{aligned} L_{ij}^{\mathrm{mod}} &= \tau_{ij}^{\mathrm{mod}}(C, \widehat{\Delta}, \widehat{\overline{u}}) - \widehat{\tau_{ij}^{\mathrm{mod}}(C, \overline{\Delta}, \overline{u})} \\ &= -(C\widehat{\Delta})^2 \widehat{\overline{\mathcal{D}_m}}\, 2\widehat{\overline{S_{ij}}} + (C\overline{\Delta})^2 \widehat{\overline{\mathcal{D}_m}\, 2\overline{S_{ij}}} \\ &= -2(C\overline{\Delta})^2 \left(\frac{\widehat{\Delta}^2}{\overline{\Delta}^2} \widehat{\overline{\mathcal{D}_m}}\,\widehat{\overline{S_{ij}}} - \widehat{\overline{\mathcal{D}_m}\,\overline{S_{ij}}}\right) \\ &= -2(C\overline{\Delta})^2 M_{ij} \quad , \end{aligned} \tag{4.16}$$

where

$$M_{ij} = \frac{\widehat{\Delta}^2}{\overline{\Delta}^2} \widehat{\overline{\mathcal{D}_m}}\,\widehat{\overline{S_{ij}}} - \widehat{\overline{\mathcal{D}_m}\,\overline{S_{ij}}} \quad . \tag{4.17}$$

Since L_{ij} and L_{ij}^{mod} have up to 9 elements respectively, the ideal situation that $L_{ij} = L_{ij}^{\mathrm{mod}}$ by simply selecting one parameter - the model constant C - is almost impossible. Therefore, several methods to find the most appropriate C have been proposed. Here we introduce the widely used Lilly's method [19] which is adopted in this work.

Lilly suggests that the square of error of physical and modeled SGS stress tensor, which is

$$Q = (L_{ij} + 2(C\overline{\Delta})^2 M_{ij})^2 \quad , \tag{4.18}$$

can be minimized using a least squares approach, and that yields

$$\frac{\partial Q}{\partial C} = 0 \quad , \tag{4.19}$$

since apparently $\partial^2 Q/\partial C^2 > 0$. So the final expression becomes

$$(C\overline{\Delta})^2 = -\frac{L_{ij}M_{ij}}{2M_{kl}M_{kl}} \quad . \tag{4.20}$$

It is worth noting that the value of $(C\overline{\Delta})^2$ given by Equation 4.20 can also be negative, since nothing on the right-hand side ensures the expression to be positive. The resulted negative ν_t is proved to be meaningful on account of the energy backscatter from fine scale to the coarse scale [20]. But generally, the positive total viscosity $\nu_{\mathrm{phy}} + \nu_{\mathrm{SGS}} \geq 0$ has to be fulfilled for the sake of the numerical stability.

4.4.2 Element-based modal filter

From the previous section, we see that a test filter is needed for the dynamic procedure. As noted in Section 2.3, modal filter which can filter signals according to their frequency components is an ideal candidate for dynamic model implementation of large eddy simulation. A low-pass filter allows low frequency components to remain, and the high-order oscillations are filtered out. For a nodal basis system such like Lagrange basis, the main problem is that the high frequency components appear in every single mode. Therefore, every mode must modified in order to filter out high frequencies. On the other hand, however, the modal filtering is very convenient for Legendre basis by just cutting off high-order modes, since the mode generation is hierarchical and high order frequencies are only stored in high order modes. In order to combine the strong points of Lagrange basis (direct access to Gauss-quadrature) and Legendre basis (convenience for modal filtering), a discrete polynomial transformation (DPT) technique is proposed and successfully implemented in the element-based filtering of high-order DG methods, see [6], [4]. This method is briefly illustrated as follows.

We denote the vector of coefficient inside the element as $\underline{u}^{\mathrm{Le}}$ and $\underline{u}^{\mathrm{La}}$ for Legendre and Lagrange basis respectively. The coefficient vectors after filtering are denoted as $\underline{\widehat{u}}^{\mathrm{Le}}$ and $\underline{\widehat{u}}^{\mathrm{La}}$. The Legendre coefficient vector applied by a modal filter should be

$$\underline{\widehat{u}}^{\mathrm{Le}} = \boldsymbol{F}\underline{u}^{\mathrm{Le}} \quad , \tag{4.21}$$

where $\boldsymbol{F}$ is the filter matrix. For sharp cut-off modal filter with cut-off polynomial order P_c, $\boldsymbol{F}$ should be a square matrix with first $P_c + 1$ elements in its diagonal filled with 1 while all other elements are 0. The filtered Legendre coefficients $\underline{\widehat{u}}^{\mathrm{Le}}$ can be transformed back to Lagrange basis $\underline{\widehat{u}}^{\mathrm{La}}$ via relationship in Equation 3.15, which is

$$\begin{aligned} \underline{\widehat{u}}^{\mathrm{La}} =& \boldsymbol{V}\underline{\widehat{u}}^{\mathrm{Le}} = \boldsymbol{V}\boldsymbol{F}\underline{u}^{\mathrm{Le}} \\ =& \boldsymbol{V}\boldsymbol{F}\boldsymbol{V}^{-1}\underline{u}^{\mathrm{La}} \\ =& \widehat{\boldsymbol{F}}\underline{u}^{\mathrm{La}} \quad . \end{aligned} \tag{4.22}$$

In this way, we have the access of filtered Lagrange coefficients $\underline{\widehat{u}}^{\mathrm{La}}$ on the identical quadrature points directly from the original Lagrange coefficients $\underline{u}^{\mathrm{La}}$. It is worth noting that the modified filter matrix $\widehat{\boldsymbol{F}} = \boldsymbol{V}\boldsymbol{F}\boldsymbol{V}^{-1}$ can be assembled in a pre-processing step and does not have to recalculated in every time-step [4].

To illustrate the effect of filtering with DPT, we take the filtering process of $P = 5$ signal by sharp cut-off filter $P = 3$ as an example, see Figure 4.1. Obviously, the filtered signal is smoother, since the high-frequency components are removed. However, we also see that the boundary values are no more preserved. This is because the Legendre basis does not have edge-inside separation property. By multi-element spectral methods, this leads to C^0 discontinuity at element interfaces. For element-based modal filter we argued, however, this should not present a problem since the filtered results only help to determine the SGS viscosity inside the element, but not be used in the time integration directly.

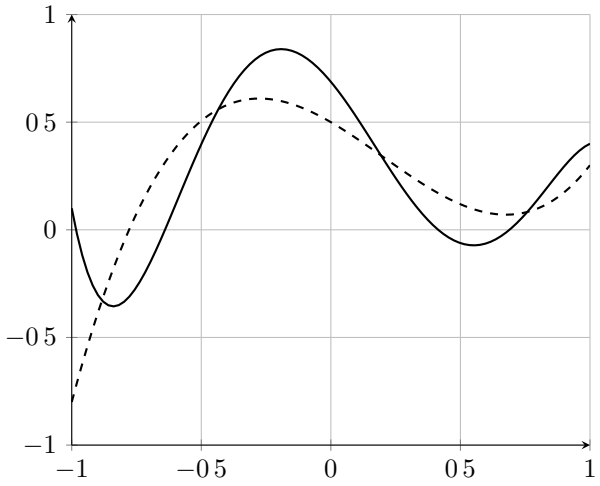

Figure 4.1: Effect of DPT: Filtering of a original function with $P = 5$ (solid line) using the sharp cut-off modal filter $P = 3$ (dashed line). Note that the marginal values are no more preserved after filtering.

4.4.3 Stabilization of the dynamic model

As mentioned in Section 4.4.1, the negative SGS viscosity resulted from dynamic procedure can cause numerical instability. Moreover, the dynamic procedure is found to be instabil particularly when dealing with strongly anisotrop turbulent flows. To reduce the variability of model constant from dynamic procedures, several stabilization techniques are introduced in the dynamic model. For example, the negative ν_t can be significantly prevented by some means of averaging, such as averaging over a small region. A practical way of realizing that under the discontinuous Galerkin method is averaging over the element, which provides a fixed constant inside the element. That

means replacing the Equation 4.20 by

$$(C\overline{\Delta})^2_{\mathrm{e}} = -\frac{1}{2}\frac{\langle L_{ij}M_{ij}\rangle_{\mathrm{e}}}{\langle M_{kl}M_{kl}\rangle_{\mathrm{e}}} \quad , \tag{4.23}$$

where $\langle\rangle_{\mathrm{ele}}$ means the spatial averaging over element. Equation 4.23 is adopted as default setting in this work. Note that since this formulation can still produce negative SGS viscosity, the total viscosity $\nu = \nu_{\mathrm{phy}} + \nu_{\mathrm{t}} \geq 0$ is rigidly fulfilled.

To completely prevent negative SGS viscosity, one can clip the remaining negative values of dynamically computed constant after averaging, which means reformulating Equation 4.23 by

$$(C\overline{\Delta})^2_{\mathrm{e}} = \max\left[-\frac{1}{2}\frac{\langle L_{ij}M_{ij}\rangle_{\mathrm{e}}}{\langle M_{kl}M_{kl}\rangle_{\mathrm{e}}}, 0\right] \quad . \tag{4.24}$$

Another practical method to reduce the oscillation of model constant in terms of time evolution is to apply recursive filter on the model constant, see the work of Breuer [21]. This filtering technique uses the constant from last time-step to stabilize the constant for current time-step

$$C^{[n+1]}_{\mathrm{modified}} = (1-\varepsilon)C^{[n]} + \varepsilon C^{[n+1]} \quad , \tag{4.25}$$

where index $[n]$ denotes the previous time-step and $[n+1]$ the current time-step. It is reported that by choosing ε in the order of 10^{-3}, most of the high frequency oscillations are damped out.

5 Validation for Taylor-Green Vortex

5.1 Three-dimensional Taylor-Green Vortex flow

The Taylor-Green Vortex (TGV) flow is considered as a prototype for validating various mechanisms and phenomena of turbulent flows, including turbulent transition, vortex stretching and production of small eddies. The boundaries of TGV are considered to be all periodic, which keep the flow in a cubic domain $[-\pi L, \pi L]^3$. Besides, no volume force is considered in this problem, e.g. $\boldsymbol{f} \equiv 0$. The initial velocity field of TGV flow which contains only single Fourier mode is given by

$$\boldsymbol{u}(\boldsymbol{x}; t=0) = \begin{bmatrix} u_x(x,y,z;t=0) \\ u_y(x,y,z;t=0) \\ u_z(x,y,z;t=0) \end{bmatrix} = \begin{bmatrix} U_0 \sin(\frac{x}{L}) \cos(\frac{y}{L}) \cos(\frac{z}{L}) \\ -U_0 \cos(\frac{x}{L}) \sin(\frac{y}{L}) \cos(\frac{z}{L}) \\ 0 \end{bmatrix} \quad ; \tag{5.1}$$

For simplicity, the initial velocity magnitude is generally set as $U_0 = 1$. Furthermore, the unit wave length $L = 1$ is also adopted. In this way, we obtain a unit characteristic convective time $t_c = L/U_0 = 1$ and the Reynolds number of TGV problem is fully decided by the dynamical (molecular) viscosity

$$Re = \frac{U_0 L}{\nu_{\text{phy}}} = \frac{1}{\nu_{\text{phy}}} \quad . \tag{5.2}$$

The initial velocity field of TGV flow with settings above is visualized in Figure 5.1.

For incompressible flow solver, the Reynolds number should be selected such that the incompressibility constraints do not influence the flow evolution essentially. For the present work, we choose the $Re = 1600$ case (corresponding to $Ma = 0.1$) as a benchmark for the following investigations. Several works [22] report that the onset of instability of Taylor-Green Vortex is around $t \approx 5t_c$, and the maximum of the dissipation appears at $t \approx 8.9t_c$. Since a unit characteristic time is adopted for our case, from now on, the time line t of diagrams also refers to normalized time t/t_c, unless stated otherwise.

Some mandatory results offer a spatially statistical evaluation of the temporal evolution of Taylor-Green Vortex flow. From the analysis of energy balance, the most important indication is the average kinetic energy on the computational domain Ω_h

$$E_k = \frac{1}{V_{\Omega_h}} \int_{\Omega_h} \frac{1}{2} \boldsymbol{u}_h \cdot \boldsymbol{u}_h \mathrm{d}\Omega \quad . \tag{5.3}$$

Furthermore, the physical (or molecular) dissipation rate, SGS dissipation rate and numerical dissi-

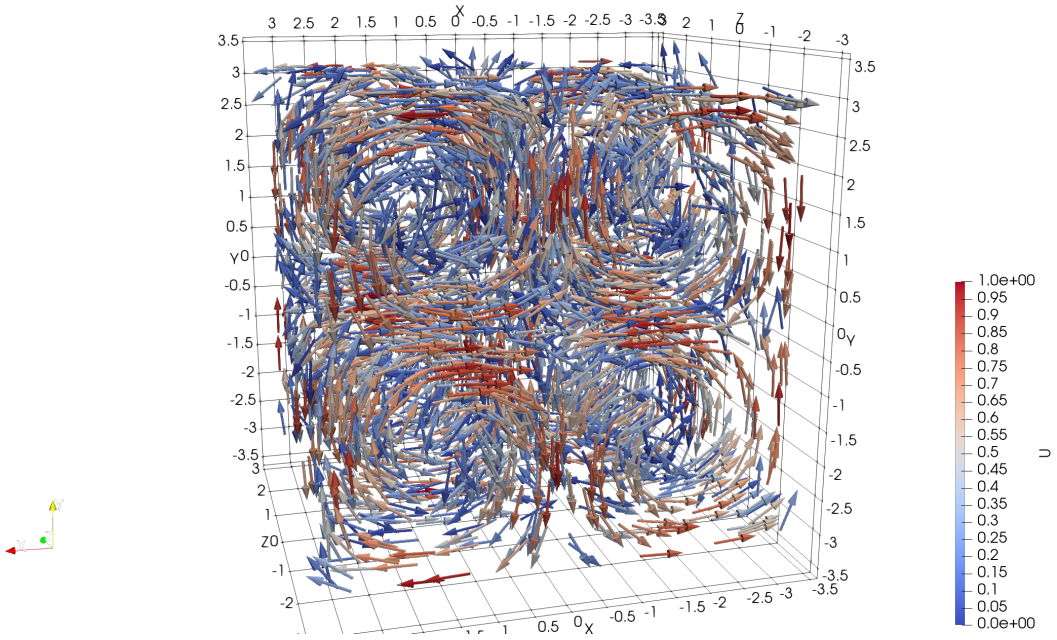

Figure 5.1: Initial velocity field ($t = 0$) of Taylor-Green Vortex flow. Arrows point to velocity ($\boldsymbol{u}$) direction, colored by velocity magnitude.

pation rate are defined as

$$\epsilon_{\text{phy}} = \frac{1}{V_{\Omega_h}} \int_{\Omega_h} \nu_{\text{phy}} \nabla \boldsymbol{u}_h : \nabla \boldsymbol{u}_h \mathrm{d}\Omega \quad ; \tag{5.4}$$

$$\epsilon_{\text{t}} = \frac{1}{V_{\Omega_h}} \int_{\Omega_h} \nu_t \nabla \boldsymbol{u}_h : \nabla \boldsymbol{u}_h \mathrm{d}\Omega \quad ; \tag{5.5}$$

$$\epsilon_{\text{num}} = -\frac{\mathrm{d}E_k}{\mathrm{d}t} - \epsilon_{\text{phy}} - \epsilon_{\text{t}} \quad , \tag{5.6}$$

where the viscosity ν_{phy} and ν_t represents molecular and SGS viscosity respectively, V the volume of computational domain, and the rate of change of kinetic energy $-\mathrm{d}E_k/\mathrm{d}t$ is the sum of all three dissipation terms. It is worth denoting that for no-model approach, ϵ_t disappears since there exists no explicit ν_t.

Regarding the spatial discretization scheme of simulations, The three-dimensional effective spatial resolution DoF in terms of element number N and polynomial order P is defined as

$$\mathrm{DoF} = [N(P+1)]^3 \quad . \tag{5.7}$$

5.2 DNS result at $Re = 1600$

Wang et al. [23] point out that a reference DNS simulation result has to have at least 256^3 DOFs. For the present work, our DNS reference is based on a computational grid of $N = 16, P = 15$ ($256^3\mathrm{DoFs}$). Despite of some more accurate results using 512^3 and 1024^3 DoFs in other works ([3], [15]), the vortex structure of our result is believed to be well resolved and sufficiently accurate as the reference.

The temporal evolution of kinetic energy E_k and its dissipation rate $-\mathrm{d}E_k/\mathrm{d}t$ up to $t = 20$ are plotted in Figure 5.2. As a reference, we have also plotted the result from Fehn et al. [3] in the same Figure, where the computational grid $N = 128, P = 7$ is employed. From it we see the dissipation peak at $t \approx 8.9$, and both curves show great agreement with the reference from Fehn et al..

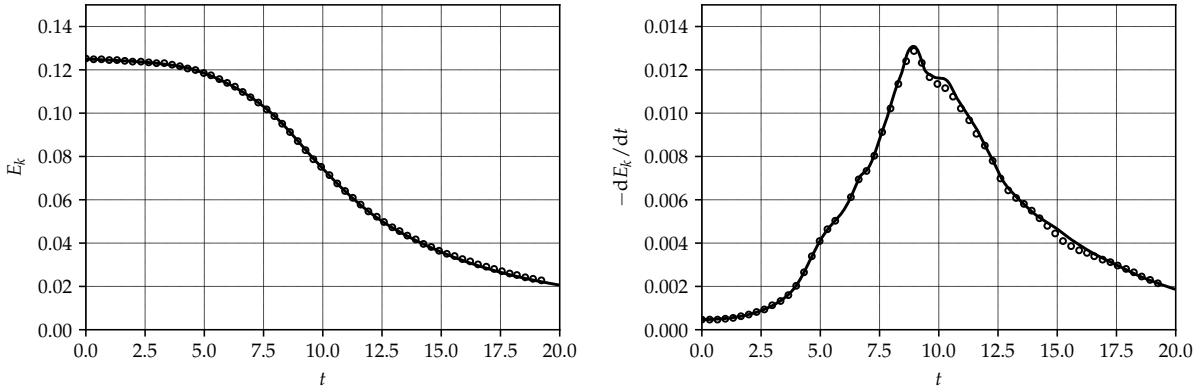

Figure 5.2: Temporal evolution of total kinetic energy E_k (left) and rate of change of total kinetic energy $\mathrm{d}E_k/\mathrm{d}t$ (right) of TGV flow. Solid line (–): DNS result obtained on computational grid $N = 16, P = 15$; Hollow circle (○): reference data of 1024^3 from Fehn et al. [3].

The temporal evolution of energy spectra from selected time is presented in Figure 5.3. It is seen that the turbulent structure of Taylor-Green Vortex develops from single large-scale mode towards small scale, and a well developed inertial range which follows Kolmogorov's $-5/3$ law is obtained at about $t = 9$, where is approximately the maximum of total kinetic energy dissipation rate.

Finally, the vortex structures after λ_2-criterion[1] from Jeong et al. [24] at $t = 5$ and $t = 11$ are illustrated in Figure 5.4, which correspond to the start of instability of TGV and a critical dissipation time we are interested in for LES simulations respectively. We can see that at $t = 5$, the large-scale vortex structure is still well organized and the TGV flow is believed to be laminar, whereas at $t = 11$ the space is occupied with small structures and the flow is already turbulent.

[1] See Appendix A.2.

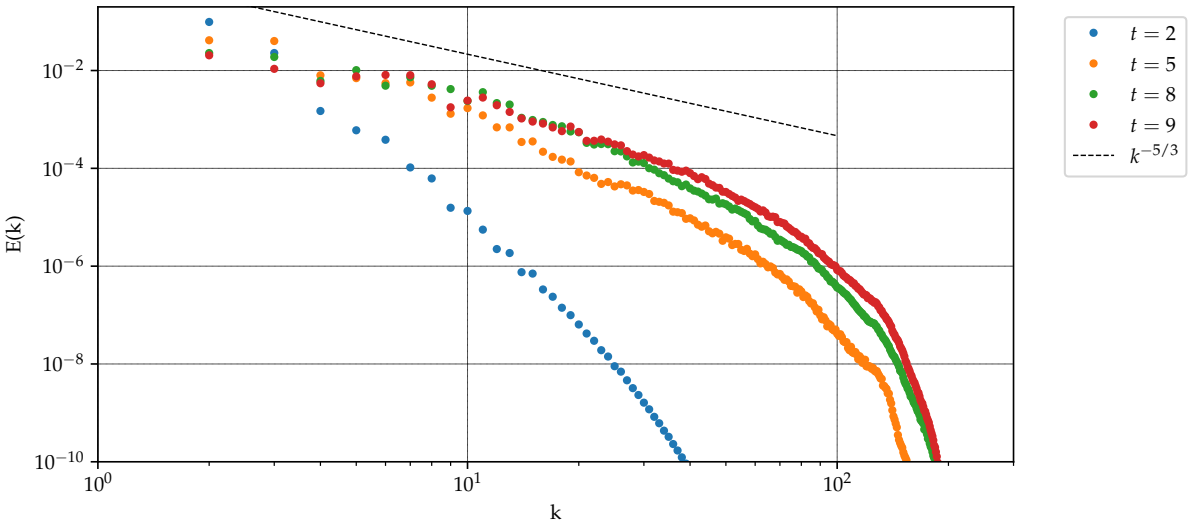

Figure 5.3: Kinetic energy spectra of TGV flow from DNS ($N = 16, P = 15$) at selected time points.

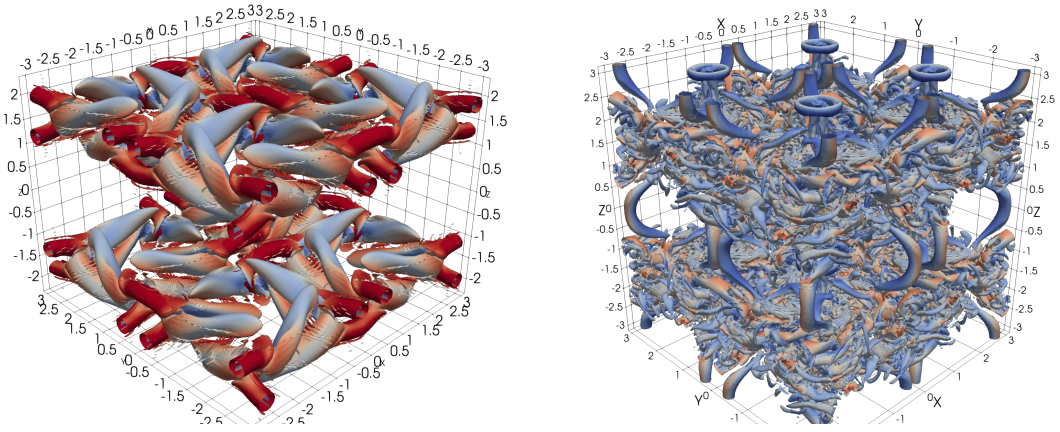

(a) $t = 5$ (b) $t = 11$

Figure 5.4: Vortex structure of TGV flow at (a) $t = 5$; (b) $t = 11$, obtained with iso-surfaces after λ_2-criterion ($\lambda_2 = -1.5$), colored by velocity magnitude in $|U| \in [0,1]$.

5.3 Computations with σ-model

5.3.1 Preliminaries

The classical static SGS model uses a predetermined model constant, which remains constant in space and time during the whole simulation. However, as noted in Section 4.4.1, the static model also shows some drawbacks which affect the accuracy of simulation. For example, it cannot recognize the laminar flow case or near wall situations and still brings unnecessary turbulent dissipation. Moreover, the model constant always need to be calibrated in terms of different flow cases as well as definitions of the characteristic length Δ. As shown in Figure 5.5, we have found that the embedding of σ-model with suggested modal constant $C_\sigma = 1.35$ leads to too much dissipation for $t < 5$, when the laminar flow motions are still well resolved under 96^3 resolution. The too little physical dissipation ϵ_{phy} for all three cases indicates that the vortex evolution is severely disturbed by early overcorrected turbulent dissipation and thus leads to an inaccurate result. Besides, we also notice that the numerical dissipations from all polynomial orders $P = 5, 7, 15$ are slightly negative, which could be an evidence that the static model with $C_\sigma = 1.5$ brings enough (or too much) dissipation already. To better understand the dissipation distribution in diagrams such as Figure 5.5, we denote that the SGS dissipation ϵ_{t} is stacked upon ϵ_{phy} such that the top of ϵ_{t} represents the sum of both dissipations. In this meaning, the difference between the line $-\mathrm{d}E_k/\mathrm{d}t$ and top of ϵ_{t} represents the numerical dissipation ϵ_{num}, which is negative if ϵ_{t} is higher than $-\mathrm{d}E_k/\mathrm{d}t$.

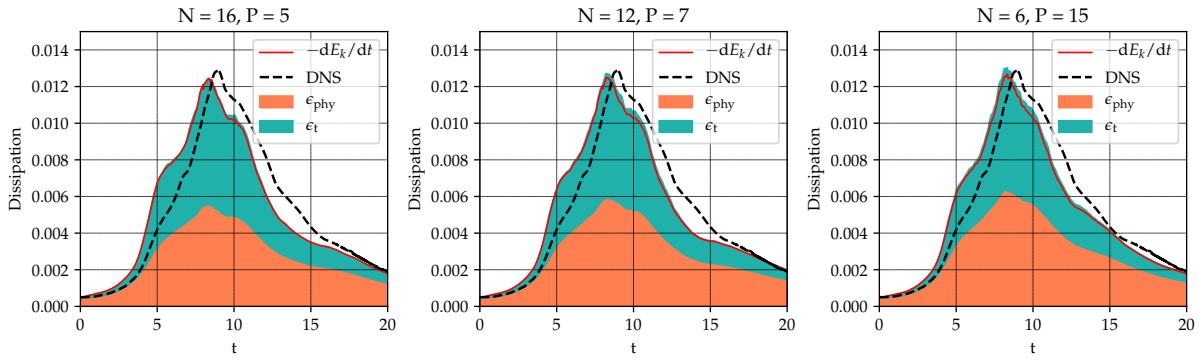

Figure 5.5: Dissipation contribution of TGV flow for static σ-model with $C_\sigma = 1.35$ under effective resolution of 96^3.

The dynamic model on the other hand provides SGS dissipation by comparing the filtered results from resolved scales and thus can automatically recognize those situations and adjust the model constant. Despite of the extra computational cost for presenting the filtering process, the dynamic model based on dynamic procedure still plays a central role since this method provides directly the model constant and is often employed to calibrate the model constant.

For the adaptation and validation purpose of σ-model in DG method, we employ both static and dynamic models for investigation. The dynamic model is based on Lilly's method (Section 4.4.1) to obtain the model constant C_σ, and the element-based modal filter in Section 4.4.2 is employed as test filter. The resulted C_σ of each point are averaged by weight over the element and thus the model constant is uniform inside the element. To ensure the stability, extra divergence and continuity penalty terms are applied in the weak formulation and thus, could bring extra dissipation which is included in numerical dissipation, since there is no counterpart of these terms in the original LES formulation. Furthermore, we use $P_c = (P-1)/2$ as the cut-off polynomial order for dynamic model simulations unless stated.

To avoid possible uncertainties of the static σ-model, we firstly investigate properties of dynamic σ-model and then try to adapt parameters to static model.

5.3.2 Towards h- and P-refinement

In this section, we investigate the property of dynamic σ-model under h- and P-refinement. As denoted in Section 4.4.1, the model constant should be consistent in terms of resolvability of vortices in inertial range. For DG method, the resolvability of vortex structures relies on two kinds of grid refinements, which are increasing the element number N (h-refinement) and increasing the polynomial order inside the element P (P-refinement) respectively. Therefore, we are interested in the behavior of dynamic σ-model under these two refinement strategies. For this purpose, we run a series of simulations with increasing effective spatial resolution (from 64^3, 96^3 to 128^3) by simply increasing element number (h-refinement) or polynomial order (P-refinement). The configuration of simulations can be found in Table 5.1.

Table 5.1: Configuration of simulations under h, P-refinement

type	64^3	96^3	128^3
h-refinement	$N = 8, P = 7$	$N = 12, P = 7$	$N = 16, P = 7$
P-refinement	$N = 16, P = 3$	$N = 16, P = 5$	

The dissipation diagrams can be found in Figure 5.6. We denote that the identical result for case $N = 16, P = 7$ is duplicated in both subfigures to make an intuitive comparison.

For both refinement strategies, we find that the total dissipation rate $-\mathrm{d}E_k/(d)t$ converges toward the DNS result with increasing spatial resolution. For h-refinement with constant polynomial order $P = 7$, it is seen that the numerical dissipation remains on a very low level and the extra dissipation for under-resolved turbulent motions is mainly contributed by ϵ_t from σ-model. Besides, the increase of element number (thus larger element interface) has only limited influence on numerical dissipation for $P = 7$. Along with a higher spatial resolution, the small-scale flow motions are better

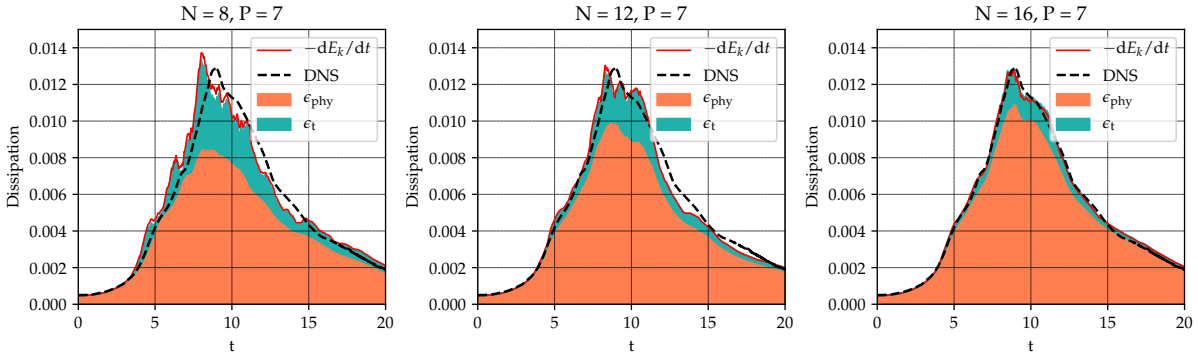

(a) h-refinement

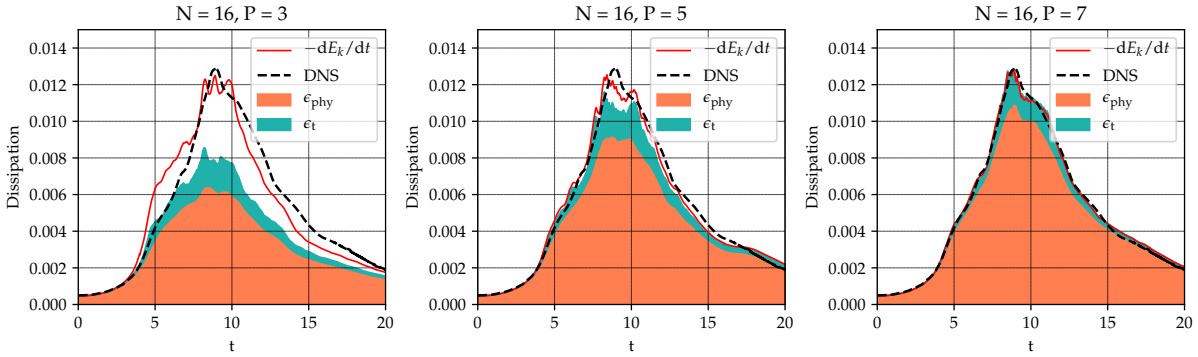

(b) P-refinement

Figure 5.6: Comparison of dissipation mechanisms for dynamic σ-model under (a) h-refinement; (b) P-refinement.

resolved. This tendency is reflected on the increasing physical dissipation rate ϵ_{phy} from $N = 8$ towards $N = 16$ while the SGS dissipation rate ν_{t} decreases continuously so that a moderate total dissipation is always reserved. Another interesting observation is that the smoothness of ϵ_t is continuously improved in the context of h-refinement.

On the other hand, different dissipation behaviors are observed for P-refinement. For $P = 3$ case, the method is obviously too dissipative for the early evolution of TGV flow until $t \approx 7.5$. Since the numerical dissipation is dominant for low order cases, the dynamic σ-model has only very limited contribution, and the resolved physical dissipation is much less than h-refinement case for 64^3. The numerical dissipation reduces rapidly by higher-order simulations, and ϵ_t resulted by σ-model gradually becomes the main contributor of extra dissipation.

In Table 5.2, we list the mean value of C_σ in time interval $t \in [12, 20]$, where the TGV flow gradually becomes quasi-isotropic and a stable temporal evolution of model constant is observed. From this table, we see that for P-refinement strategies, the model constant increases remarkably in terms of higher polynomial order P. Considering the great differences of numerical dissipation

Table 5.2: Mean value of C_σ for $t \in [12, 20]$

type	64^3	96^3	128^3
h-refinement	0.46	0.49	0.43
P-refinement	0.30	0.36	

under different polynomial order, we believe that the for no-model approach introduced numerical dissipation do have a great influence on the behavior of dynamic σ-model. On the other hand, the value of C_σ under h-refinement shows a better consistency, whereas no general rule for the change of C_σ is observed.

5.3.3 Effect of cut-off polynomial order

When we use the element-based modal filter to obtain the filtered velocity components on the test grid, a new parameter - the cut-off polynomial order P_c - appears in the dynamic procedure which determines the filter identity. Unlike the dynamic procedure in classical FV approaches where $\widehat{\Delta}/\bar{\Delta} = 2$ is applied as default setting, the choice of P_c for high-order methods is more flexible since setting $\widehat{\Delta}/\bar{\Delta} = 2$ can not bring computational convenience any more. Moreover, the stability and accuracy of dynamic model depends strongly on the filtering procedure which highlights the significance of P_c, particularly when the polynomial order of simulation becomes higher. To find out the relationship between simulation quality and parameter P_c, we take LES simulations with computational grid $N = 6, P = 15$ (96^3) and different P_c from 2 to 12 as example.

The plots of dissipation rates are presented in Figure 5.7. The best possible approximation for the maximum dissipation at $t \approx 8.9$ is found in $P_c = 2$, although there exists only tiny difference between $P_c = 2$ and $P_c = 4$. When P_c gets higher, we see a clear tendency that the peak of dissipation rate shifts to $t \approx 8.5$ which is more and more overcorrected. Together with the overcorrection, the share of physical dissipation rate ϵ_{phy} is reduced whereas the SGS dissipation ϵ_{t} turns to be more and more fluctuant. It is obvious that for low P_c simulations, there exist more vortex structures although we do not know yet whether they belong to original TGV structures or just the numerical noise. The difference of ϵ_{t} among all P_c becomes obvious after $t \approx 5$ when the instability of TGV occurs and the effect of σ-model starts to get involved. Those who own higher P_c always react earlier and stronger to the transition, brings too much extra dissipation before $t = 5$ however. We denote that the TGV flow is still strongly anisotropic until $t \approx 12$, which can be a potential reason for the fluctuation by dynamic procedure when P_c gets closer to P, while the tolerance of velocity fluctuation becomes smaller. In one word, those simulations with P_c closer to P are more sensitive but more unstable to the flow transitions. Apart from all the differences however, the contributions of numerical dissipation ϵ_{num} remain insignificant, although they are all negativ most of the time.

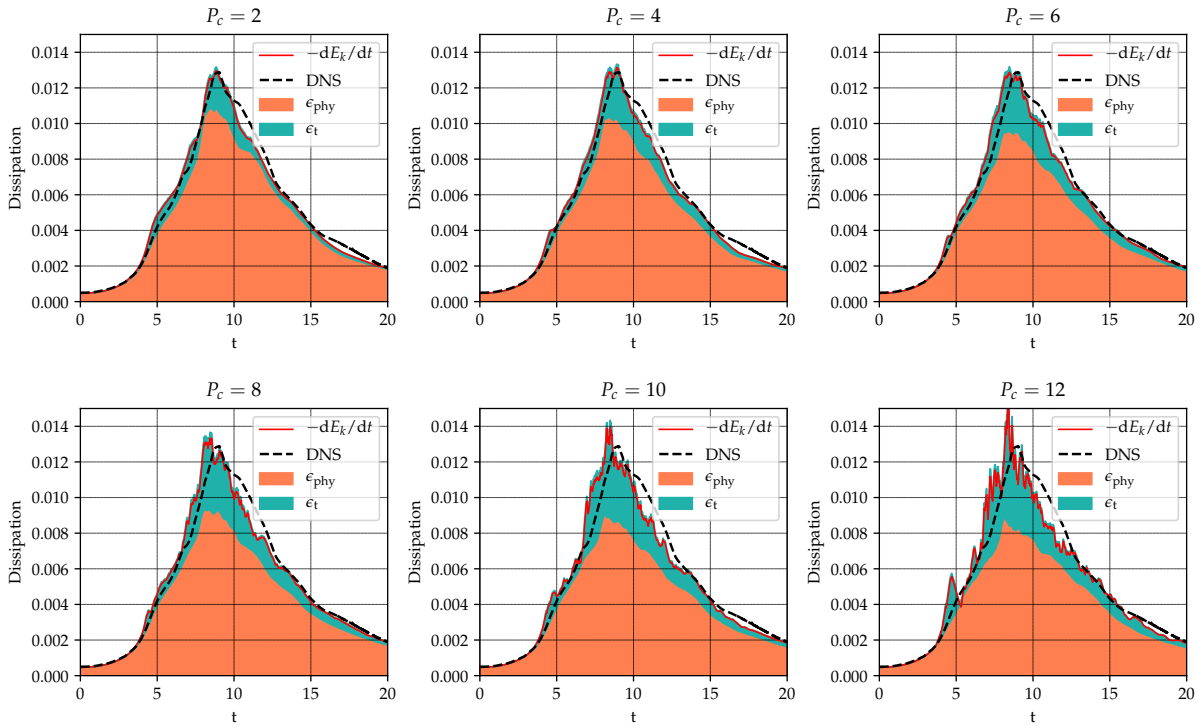

Figure 5.7: Dissipation contribution for dynamic σ-model under different cut-off polynomial order P_c by $N = 6, P = 15$.

To make sure whether the dissipation fluctuation have an influence on turbulent structure, we take the snapshot of energy spectrum for $t = 9$ which corresponds to the maximum dissipation point. As shown in Figure 5.8, the energy distribution from all P_c show good agreement with each other as well as with the DNS result within large scale range up to $k = 12$, which means that the development of large vortices are free of the choice of P_c. Meanwhile, for smaller vortices (larger wave number k), the difference becomes recognizable. Generally, those simulations with lower P_c own more energy in small-scale range, which brings more physical dissipation as shown in Figure 5.7. Compared with DNS simulation, we see that although the difference among all P_c is still hard to distinguish, the best approximation of inertial range $k = 11 \cdots 17$ is observed at higher P_c simulations, particularly at $P_c = 12$. Again, we emphasize that overall energy distribution for all P_c suits DNS results well and local difference is not the clear evidence for judging which one is better.

The energy spectra only shows the statistic consistency of turbulent structures, while the distribution of vortices can still be different. To provide a more detailed view of small-scale structures, we present the λ_2-contour of $P_c = 2$ and $P_c = 12$, which represents the most and least small-scale energy respectively (Figure 5.9). From the comparison we can see that although the main vortex structures are the same, there exists some small noisy structures for $P_c = 2$ which are unphysical compared to the DNS results. In this meaning, a higher P_c is advantageous for reducing noise and

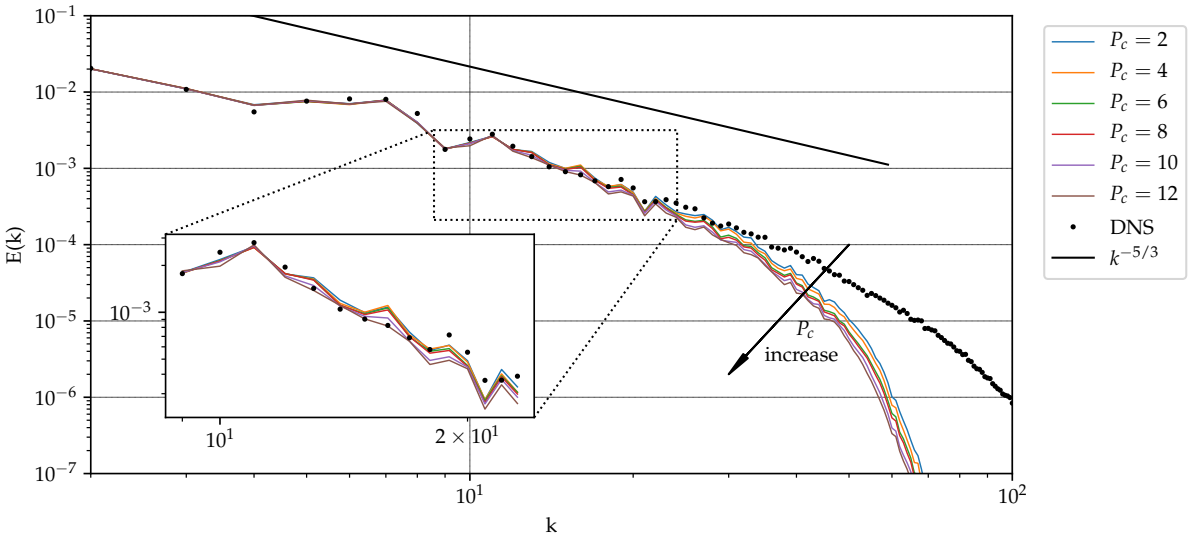

Figure 5.8: Energy spectra of TGV flow at $t = 9$, obtained by dynamic σ-model with different P_c on computational grid $N = 6, P = 15$.

keep fidelity for dynamic σ-model. Considering the instability when P_c gets closer to P, the cut-off polynomial order should be selected neither to high nor to low to balance their strong points and drawbacks.

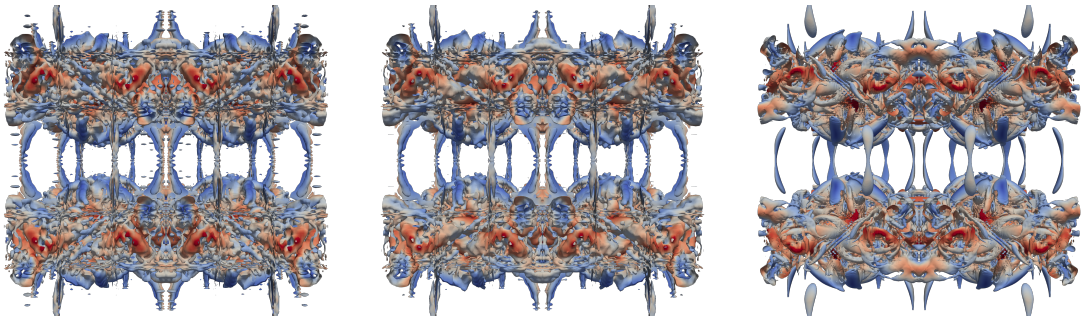

(a) $P_c = 2$ (b) $P_c = 12$ (c) DNS

Figure 5.9: Comparison of vortex structures at $t = 9$: results from dynamic σ-model with $P_c = 2, 12$ and DNS. Iso-surfaces obtained with $\lambda_2 = -1.5$, colored by velocity amplitude $|U| \in [0, 1]$.

5.3.4 Influence of spatial discretization

Now we will focus on the effect of dynamic σ-model compared with no-model simulations on the LES-grid. As discussed in Section 2.5 , the under-resolved turbulent flow simulations (or ILES) uses the dissipation effect of numerical flux to stabilize the main flow. For DG methods with higher order, the lack of numerical dissipation makes the accuracy of no-model approach questionable. To

investigate the effect of dynamic σ-model from low to high polynomial orders, we select the spatial resolution of 96^3 with three polynomial degrees : $N = 16, P = 5$; $N = 12, P = 7$ and $N = 6, P = 15$ for both approaches.

The temporal evolution of dissipation curves is shown in Figure 5.10. For both approaches, the total kinetic energy change rate for all polynomial orders is acceptable, and we do not see obvious difference among all three discretization methods under the fixed resolution. However, for resolved physical dissipation ϵ_{phy}, different behavior is shown for different approaches. For no-model simulations, the numerical dissipation is continuously decreasing and the missing part is compensated by increased physical dissipation. In some periods of time, ϵ_{phy} is even larger than the DNS reference (for example, $P = 15$ case at $t = 11$). This level of ϵ_{phy} is beyond our expectation since we know that the TGV flow is not sufficiently resolved on the LES-grid and the physical dissipation should be lower than DNS anyway. For the dynamic σ-model on the other hand, the lacking numerical dissipation by higher P is compensated by increasing SGS dissipation rate ϵ_{t}, whereas the ϵ_{phy} does not change too much. Although ϵ_{t} shows some fluctuations for all three cases, the physical dissipation remains stable. Moreover, ϵ_{num} for every mesh are found to be lower than the no-model approach, since it is partially substituted by the effect of σ-model.

Concerning the energy distributions for both approaches, we present the kinetic energy spectra at t = 9 and t = 11 (Figure 5.11). For t = 9 in Figure 5.11(a), there exists almost no difference between two approaches as well as the DNS reference particularly in large-scale range, which indicates that replacing the numerical dissipation by σ-model brings the same effect as no-model approach. The difference starts to be recognizable in the middle of inertial range, and the no-model approach which owns a higher physical dissipation rate at t = 9 (Figure 5.10) exhibits a higher energy from small eddies. For the cases with higher polynomial orders $P = 7, 15$, we find that by no-model simulations, the increasing ϵ_{phy} is mainly caused by the increasing of small-scale energies. In this way, a wider inertial range is obtained, although the pile-up of energy could be a reason of that. The dynamic σ-model on the other hand provides a relative stable energy distribution by means of polynomial order and thus shows a larger difference from no-model simulations with increasing P.

For the energy spectra at t = 11, where the second peak of ϵ_{phy} by no-model approach appears, we find that the difference between both approaches becomes larger compared with t = 9. Once again, we find that the difference is concentrated on small-scale vortex structures, which confirms that the increasing ϵ_{phy} for no-model simulations with higher polynomial orders is caused by increasing high frequency energy. For $P = 15$, we can see slight pile-up pile-up of energy from no-model approach in the inertial range compared with reference spectrum. In contrary, The energy distribution observed with dynamic σ-model shows a good consistency in terms of polynomial order, which means that more high frequency energy is dissipated by the σ-model when P gets higher.

The λ_2-contour provides a more detailed view of spatial distribution of vortices for both approaches.

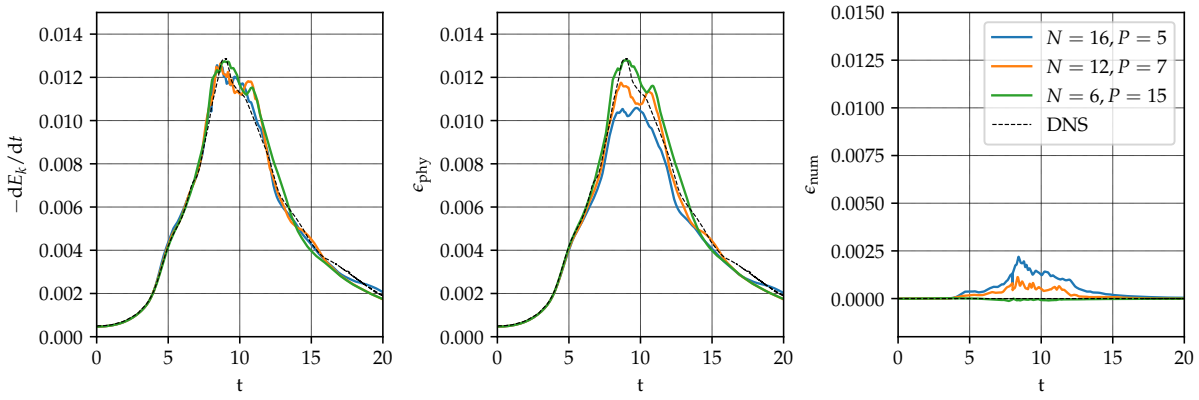

(a) No-model

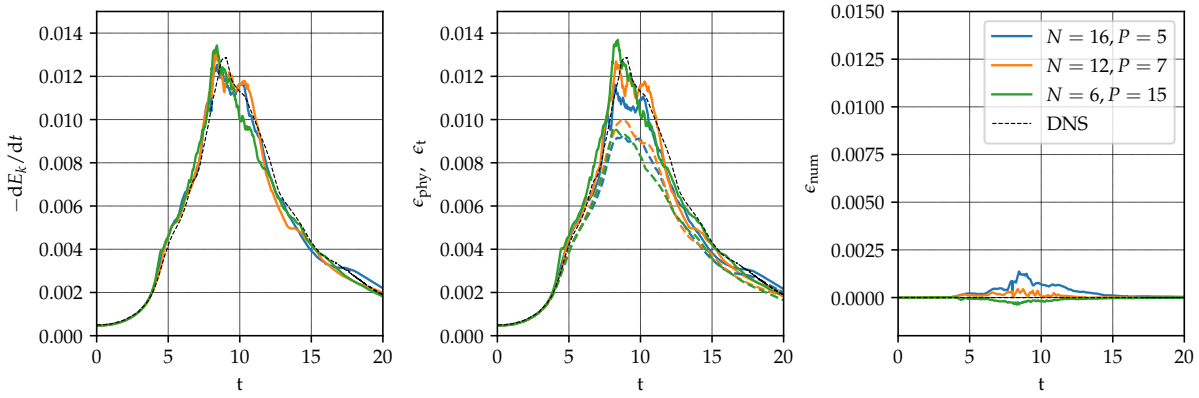

(b) Dynamic model

Figure 5.10: Dissipation distribution under different spatial discretization strategies from no-model (top) and dynamic σ-model (bottom) simulations. In each column: rate of change of kinetic energy (left), physical (and SGS) dissipation rate (middle) and numerical dissipation rate (right). For bottom middle: dashed line for physical dissipation (ϵ_{phy}), solid line for physical and SGS dissipation ($\epsilon_{\mathrm{phy}} + \epsilon_{\mathrm{t}}$).

In Figure 5.12, the iso-surfaces of vortex tubes at $t = 11$ according to λ_2-criterion are presented. For no-model approach, we can see that with increasing polynomial orders, more and more noisy vortex structures appears corresponding to the increasing ϵ_{phy} shown in Figure 5.10(a), which are unphysical compared with DNS results (Figure 5.4). Particularly by $P = 15$ case, the numerous small-scale vortices cover the main structure and the benefit using higher order techniques is difficult to follow. On the other hand, the vortex structure of dynamic σ-model shows good consistency regarding to the increasing polynomial orders. The noisy small structures by no-model approach are well dissipated and a smoother vortex structure is obtained. Furthermore, we see the continuous improvement of vortex structure presentation with increasing polynomial order. To be specific, with increasing P, the discontinuous vortex tubes observed by $P = 5$ are expanded and connected which each other such that the vortex structure is visually closer to DNS results. We denote that by higher

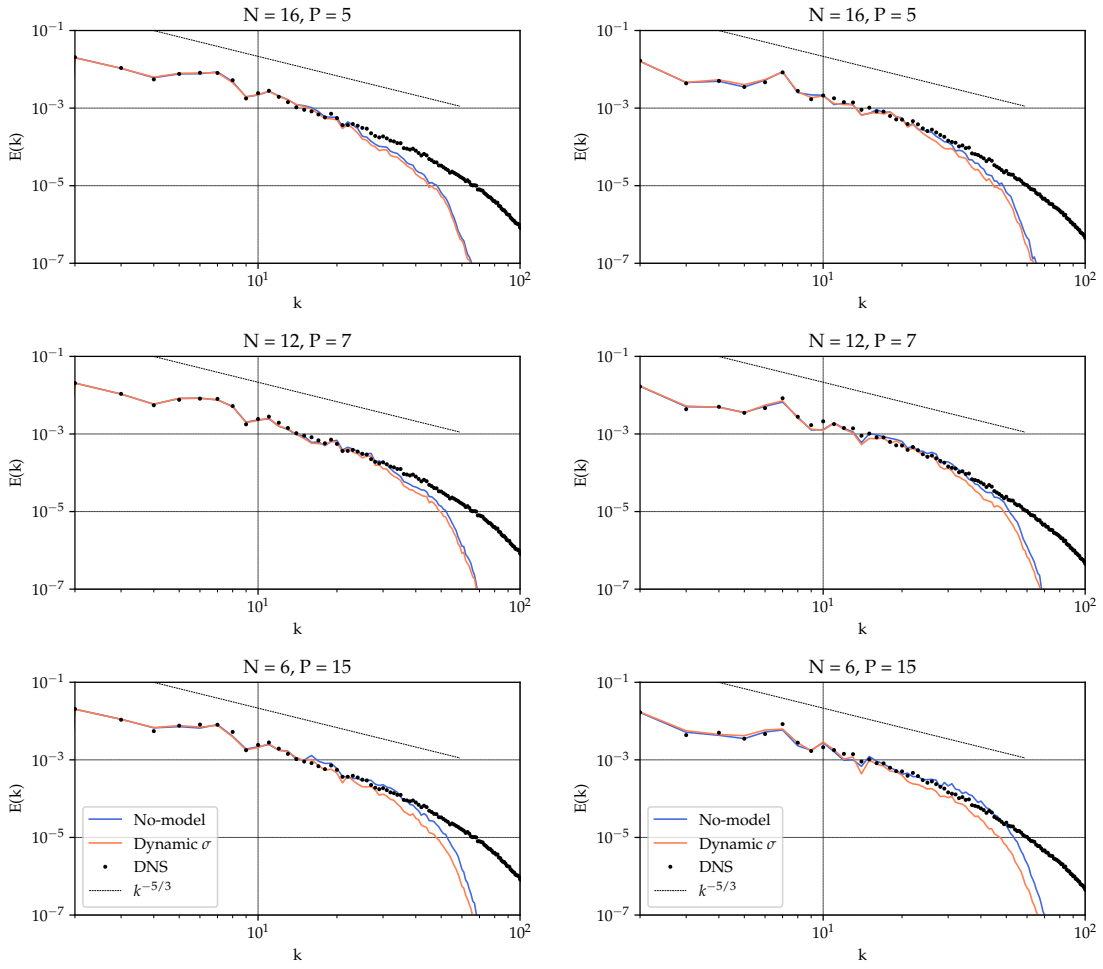

(a) t = 9 (b) t = 11

Figure 5.11: Energy spectra of no-model and dynamic σ-model simulations at (a) $t = 9$ and (b) $t = 11$. Labels valid for all figures.

Reynolds number where the effect of SGS dissipation is much larger, the difference between both approaches should be even more obvious.

5.3.5 Back to the static σ-model

In the previous sections, we have discussed the properties of dynamic σ-model under different spatial discretization schemes and filtering parameters. More frequently, the static model constant is needed to maintain the simplicity and clearness of LES simulation. In this section, we try to transfer the experiences from dynamic model to the static version. For this purpose, we take the same discretization configurations as in Section 5.3.4, namely effective resolution 96^3 with $P = 5$, 7 and 15.

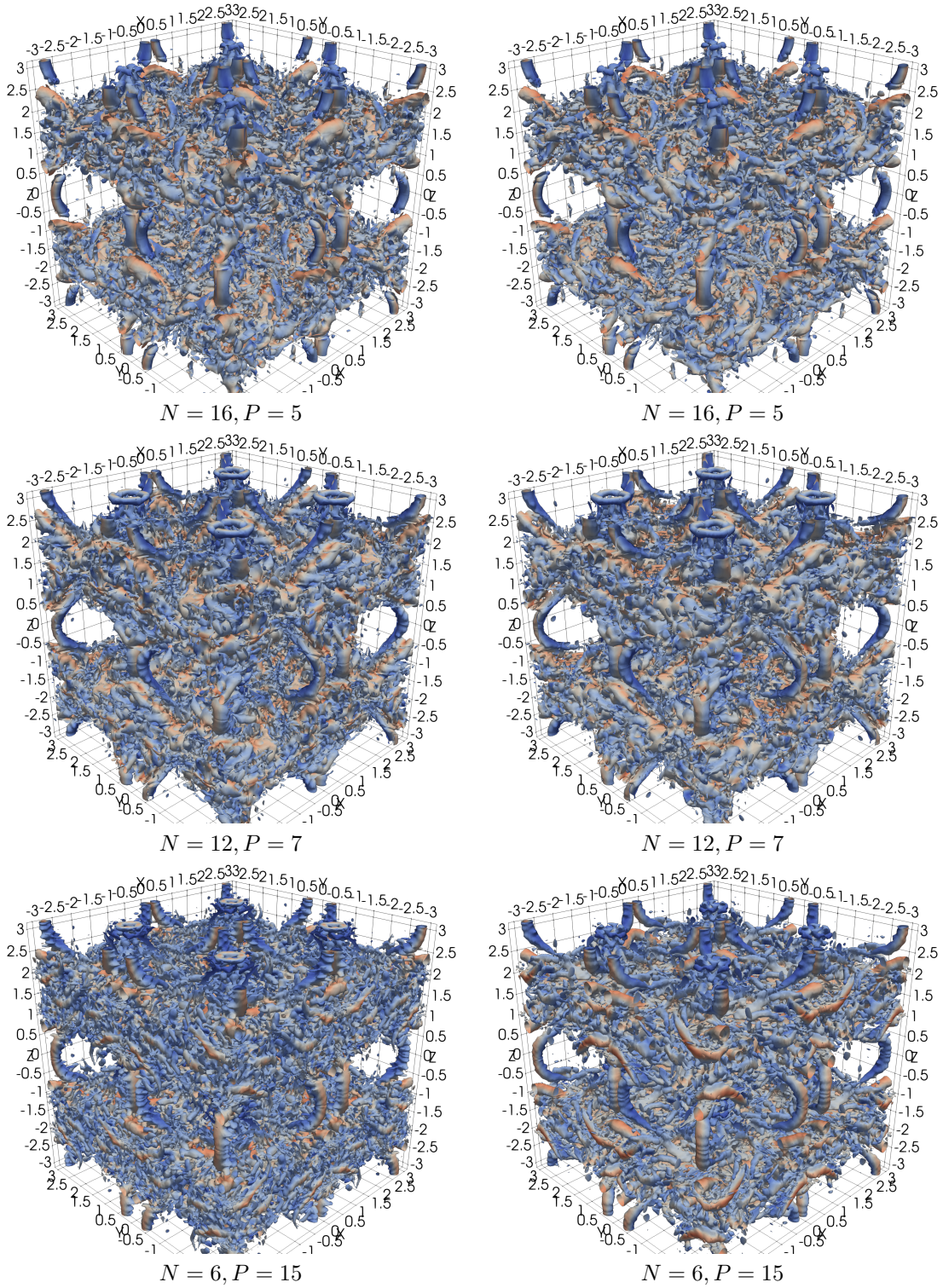

$N = 16, P = 5$ $N = 16, P = 5$

$N = 12, P = 7$ $N = 12, P = 7$

$N = 6, P = 15$ $N = 6, P = 15$

(a) No-model (b) Dynamic σ-model

Figure 5.12: λ_2-contour for (a) no-model; (b) dynamic σ-model simulations at $t = 11$. Results obtained with $\lambda_2 = -1.5$, colored by velocity amplitude $|u| \in [0,1]$.

As noted in Section 5.3.1, the model constant for static σ-model should be reevaluated to meet the current definition of characteristic length Δ. It is worth noting that for every definition of Δ, although the model constant C_σ is reserved during the simulation process, it is still indeterminate regarding to the combination of h and P. That means for every spatial discretization configuration, we must evaluate the model constant separately. To find the moderate model constant, we ran some preliminary simulations with dynamic model and the resulted time-varying mean value of C_σ over the whole computational domain is presented in Figure 5.13.

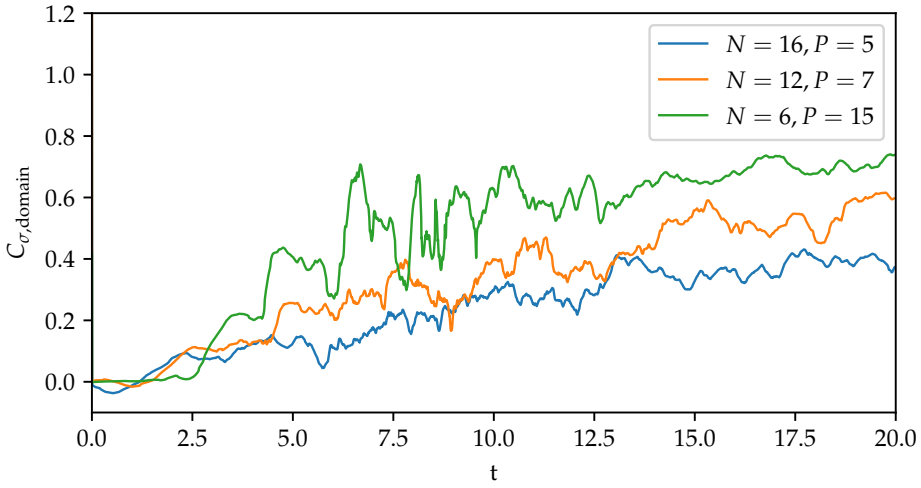

Figure 5.13: temporal evolution of C_σ from dynamic procedure for 96^3.

Obviously, the resulted model constants shows dependency on discretization parameters. For higher polynomial order, we obtain a larger model constant. Note that the SGS viscosity ν_t is not the only participant of extra dissipation, C_σ could also be affected by the change of numerical dissipations. With the presence of stronger numerical dissipation in low-order simulations, the SGS dissipation could be restrained since the resolved velocity field is already dissipated by numerical errors. We also find that for high-order schemes, the oscillation of C_σ in time is also stronger, which indicates that extra smoothing techniques might be necessary for high orders.

To determine an appropriate C_σ for the static σ-model, we take the time-averaged model constant from Figure 5.13 after $t = 10$, where the vortices are sufficiently developed and the C_σ becomes stable over time. The resulted C_σ are listed in Table 5.3 and will be adopted in static model simulations.

Table 5.3: The average of C_σ for each discretization from $t = [10, 20]$

	$N = 16, P = 5$	$N = 12, P = 7$	$N = 6, P = 15$
$C_{\sigma,\text{domain}}$	0.35	0.47	0.66

From the simulation results (Figure 5.14) using predetermined C_σ in Table 5.3, we can see a remark-

able improvement compared with suggested $C_\sigma = 1.35$. The total energy dissipation rate $-\mathrm{d}E_k/\mathrm{d}t$ for all three cases are no more overcorrected before $t \approx 5$, and it also follows DNS results better after $t = 9$, through which we believe that the vortex structures are well developed throughout the simulation. Besides, we also find that the resolved physical dissipation rate ϵ_{phy} shows good agreement with dynamic model, while the oscillation of ϵ_{t} by dynamic model is improved.

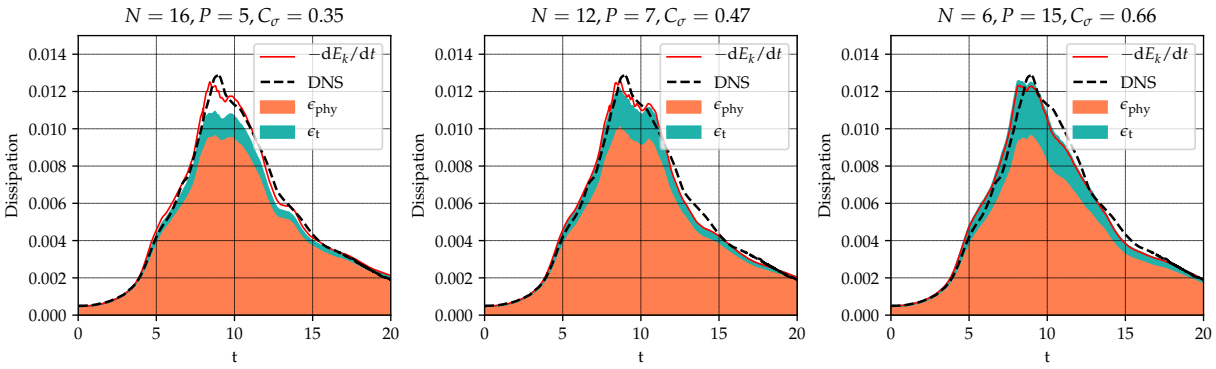

Figure 5.14: Dissipation distribution of adapted static σ-model for 96^3.

In Figure 5.15, the energy spectra with adapted static σ-model at $t = 9$ and $t = 11$ are presented. It is seen that for both cases, the results from static model agree with DNS reference in the large-scale range but a little too dissipative in small-scale range. Moreover, the energy distributions of different P are very close to each other, and the difference between static and dynamic model is hardly distinguishable. Therefore, it is believed that the adapted static C_σ works as well as a time- and space-varying constant.

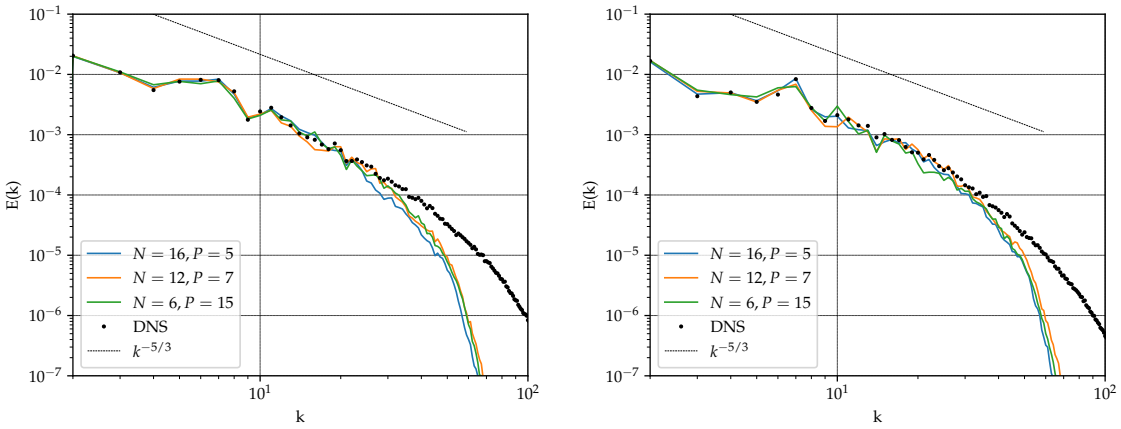

(a) $t = 9$ (b) $t = 11$

Figure 5.15: Energy spectra of TGV flow with adapted static σ-model at (a) $t = 9$ and (b) $t = 11$.

5.4 Performance

In the former sections, we have argued that the implemented σ-model shows its superiority compared with no-model approach, especially by high-order simulations. However, the additional σ-model is naturally associated with extra computational costs. We wonder whether the advantages brought by σ-model is worth putting additional computational time, particularly in the scenario of DG approach and parallel computing. To be specific, we are going to investigate the proportion of computational cost for performing σ-model in the whole simulation in this section. To do this, we test three spatial discretization schemes under 96^3 with no-model, static σ-model and dynamic σ-model respectively. As an additional dimension, parallel efficiency (different MPI processes) will also be evaluated. To minimize random error from the simulation environment, each configuration is repeated 3 times to acquire the average computation time. We denote that all the evaluation possibilities are deactivated to ensure performance.

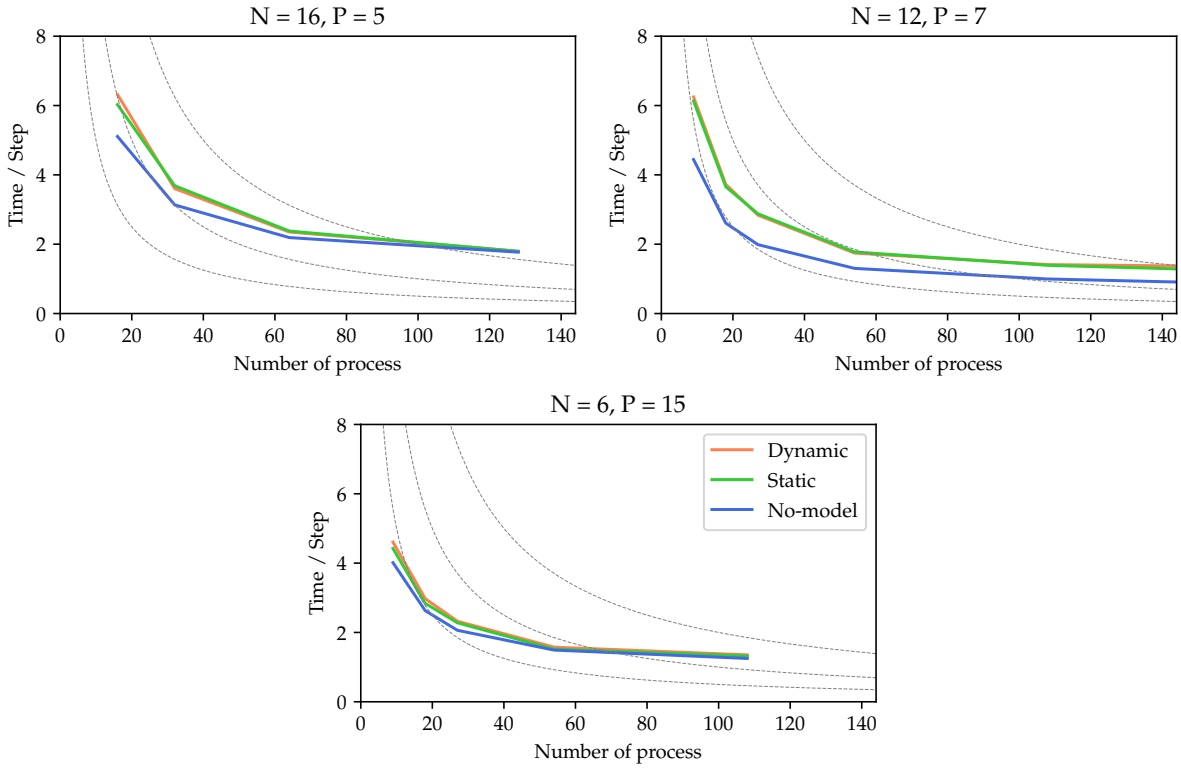

Figure 5.16: Performance overview for effective spatial resolution 96^3 with different polynomial orders. Dashed line: ideal speed-up iso-lines for pure parallel computations. Labels are valid for all subfigures.

An overview of performance (time per step) in terms of number of MPI processes is illustrated in Figure 5.16. The implementation of dynamic σ-model exhibits an additional computational cost by every time step which reduces when more processes are engaged. The reduced computational

cost is expected since the computation of dynamic procedure is an in-element behavior which is complete parallelizable and no data exchange among MPI processes is needed. For large number of processes where the serial part of program as well as the increasing communication costs becomes the bottleneck of performance, the extra cost from σ-model turns to be insignificant. Besides, we also find that for the same effective spatial resolution, both no-model computations and computations with σ-model need less computation time per time step with increasing polynomial order. Considering that we take a smaller time-step size for higher order simulations, the overall computation time should be very close.

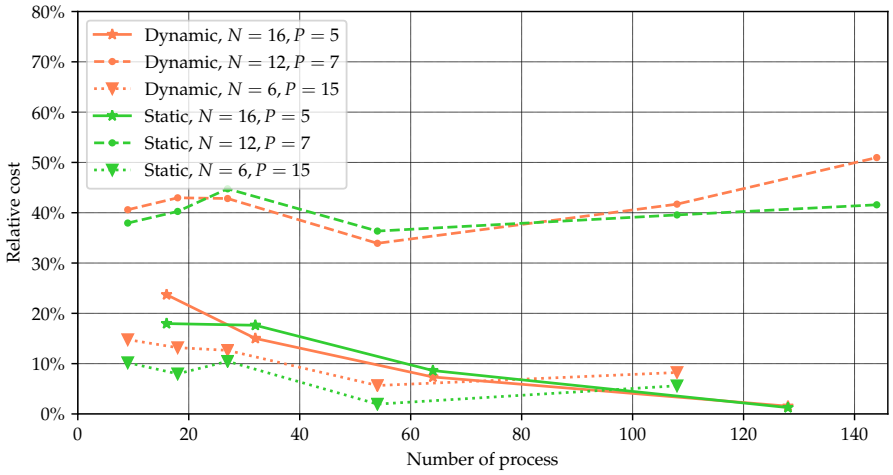

Figure 5.17: Relative cost of σ-model (%) per time step.
Relative cost = additional cost of σ-model / cost of no-model approach.

From the perspective of relative cost (Figure 5.17), it is seen that the implementation of σ-model generally brings less than 20% extra computational costs per time-step. Moreover, the static model is less costly than the dynamic model for $P = 15$, which is understandable because the dynamic procedure is not involved. However, for $P = 5$ and $P = 7$, the static σ-model requires almost as much additional cost as the dynamic one. Moreover, some exceptions are observed especially for $P = 7$ case. The no-model computations with this order show an extraordinary parallel efficiency which is the best over all cases, while the additional σ-model seems to be much more expensive (around 40%) compared with others. It is worth denoting here that although the computational cost of σ-model, including both static and dynamic model is relative stable, it can still influence other procedures beyond σ-model itself. For example, the variable viscosity inside the element caused by σ-model can lead to more iteration steps in the projection solver, which is unpredictable for different polynomial orders.

5.5 Stabilization of dynamic σ-model: clipping and temporal smoothing

As discussed in Section 4.4.1, there are several methods to overcome the stability issue of dynamic procedure in both space and time. Until now, we have only used the element-averaging to reduce the variability of C_σ in space. However, the dynamic σ-model still shows fluctuation behaviors in some certain cases particularly during the temporal evolution. In this section, we will test the stabilization effect of other two candidates (clipping and temporal smoothing) which are widely used for complex geometries.

The ”clipping” method clips the remaining negative values of dynamically calculated constant after some means of space averaging. Therefore, the model constant C_σ as well as the resulted SGS viscosity are all non-negative in space and time, and the energy backscatter from small scale to large scale is blocked. From Figure 5.14 we can see that the negative C_σ appears mainly in early stage of TGV ($t < 5$) and in low order simulations. Considering that the TGV flow is still laminar and the influence of dynamic σ-model is limited, the extra clipping operation should not have a significant influence on the simulation result. In Figure 5.18, we present the comparison of simulations for $N = 16, P = 5$ with and without clipping. For dissipation contributions in Figure 5.18(a), we can hardly recognize the difference between two methods via human visual system. Particularly, the introduction of clipping does not influence the physical dissipation (and thus the development of turbulent structures) during the whole period of time which means that the negative C_σ is sufficiently small after spatial averaging (in element) and clipping them to zero does not bring real distinction on the simulation result. Of course, we expect a more obvious effect of clipping for larger element number N, where each element becomes smaller and more negative C_σ remain after averaging.

However, the different behavior of C_σ for both methods (Figure 5.18(b)) at the very beginning of simulation draws our attention. For the case without clipping, the simulation starts up with C_σ in near-zero area, whereas by clipping the start-up C_σ is very large and drops quickly after several time-steps. This phenomenon indicates that for σ-model, the starting phase might be critical and there might be a large amount of negative C_σ. To illustrate the problem, we present the distribution of model constant from all elements at the very beginning of simulation for $N = 8, P = 7$ in Figure 5.19. From the diagram we can see that at the starting phase of TGV flow, the σ-model shows a dispersed distribution of model constants whose range is much larger than any rational values. Therefore, the clipping of negative constants moves the domain-averaged C_σ from near-zero area to a high level. We denote that the TGV flow is initially a two-dimensional flow, by which the σ-model provides zero (or very small due to the truncation error) SGS viscosity as discussed in Section 4.2. On the other side, the filtering by dynamic procedure still works well for two-dimensional flow and suggests additional dissipation that should be brought by σ-model. Therefore, at the initial

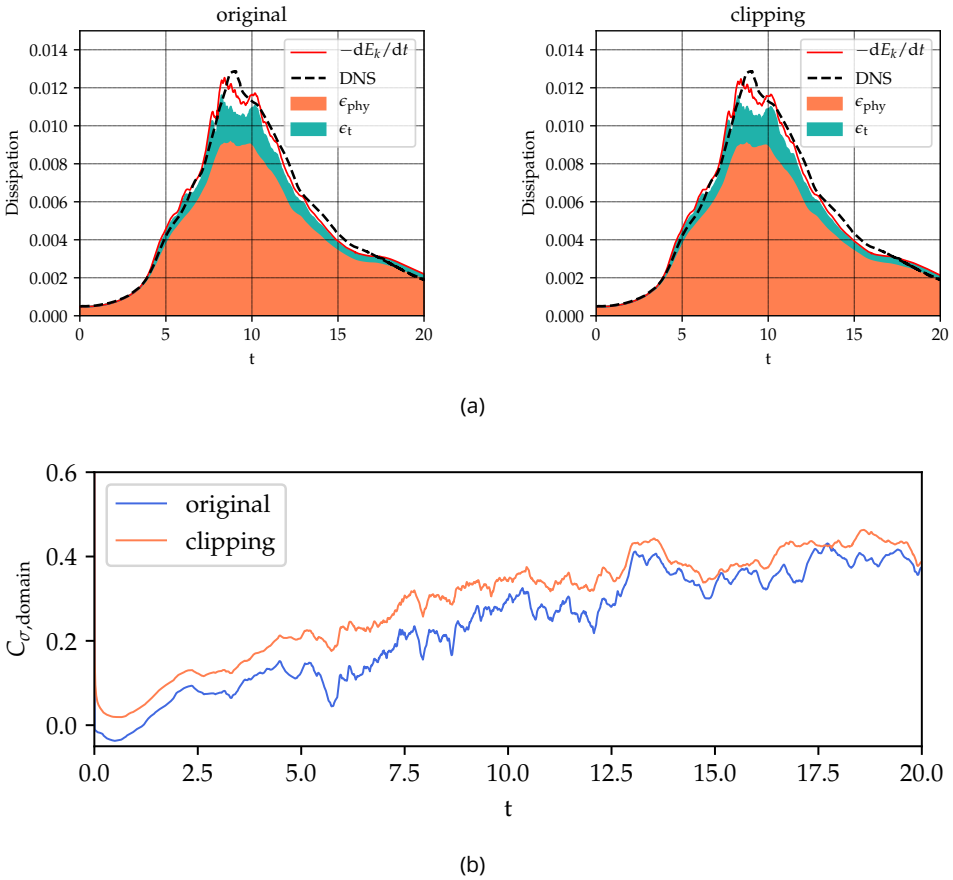

Figure 5.18: Effect of clipping: comparison of (a) dissipation and (b) temporal evolution of C_σ for original and clipping simulations under $N = 16, P = 5$.

period of approximation, the resulted C_σ values is mainly governed by numerical errors and a wide distribution is thus possible. Besides, we also find that this start-up issue is fixed as the dispersion of constants converged to near-zero area after a short period of start-up.

Although the starting issue has almost no influence on the further development of simulation, it becomes troublesome when temporal smoothing is introduced. The temporal smoothing procedure aims to filter out high-frequency oscillations in time, which will block the convergence process of C_σ to zero and keep the model constant at high level. A practical solution for this is to involve temporal smoothing procedure after the starting period. Weakness of this method is that the "starting period" has to be manually defined and re-determined for other cases than TGV problem, which is difficult to generalize.

Although the model constant at the beginning can be large, the resulted SGS viscosity ν_t remains negligible. This finding motivates us to use an alternative version of temporal smoothing which

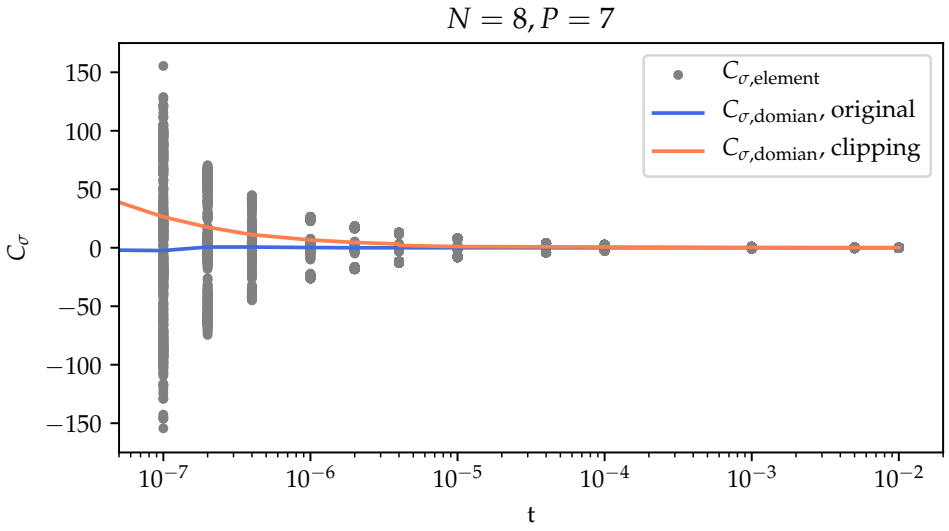

Figure 5.19: Start-up issue of dynamic σ-model: distribution of element-based C_σ and its average over entire computational domain with/without clipping.

works not on C_σ, but on the entire ν_t

$$\nu_{t,\text{modified}}^{[n+1]} = (1-\epsilon)\nu_t^{[n]} + \epsilon\nu_t^{[n+1]} \quad , \tag{5.8}$$

which is equivalent to the following expression since the characteristic length Δ does not vary with time and $\mathcal{D}_\sigma$ is parameter-freely determined for every time-step

$$(C_{\sigma,\text{modified}}^2\mathcal{D}_{\sigma,\text{e}})^{[n+1]} = (1-\epsilon)(C_\sigma^2\mathcal{D}_{\sigma,\text{e}})^{[n]} + \epsilon(C_\sigma^2\mathcal{D}_{\sigma,\text{e}})^{[n+1]} \quad . \tag{5.9}$$

Therefore, the final expression of modified constant reads

$$C_{\sigma,\text{modified}}^{[n+1]} = \text{sign}(\mathcal{C}_m)\ \sqrt{|\mathcal{C}_m|} \quad , \tag{5.10a}$$

$$\mathcal{C}_m = \frac{(1-\varepsilon)(C_\sigma^2\mathcal{D}_{\sigma,\text{e}})^{[n]} + \varepsilon(C_\sigma^2\mathcal{D}_{\sigma,\text{e}})^{[n+1]}}{\mathcal{D}_{\sigma,\text{e}}^{[n+1]}} \quad , \tag{5.10b}$$

where "$^{[\,]}$" refers to the time-step indices in order to distinct from exponents. We denote that the sign of expression inside the root is taken in front ($\text{sign}(\mathcal{C}_m)$) such that the negative modified constant is enabled. Besides, the $\mathcal{D}_{\sigma,\text{e}}$ here is a mean value of all points inside the element.

Using temporal smoothing from Equation 5.10 with $\varepsilon = 5 \cdot 10^{-3}$, we obtain the results as shown in Figure 5.20. From the dissipation diagrams in Figure 5.20(a), we see a significant improvement of stability of SGS dissipation brought by temporal smoothing. In this way, the total dissipation rate $-\text{d}E_k/\text{d}t$ is also closer to the DNS reference. Meanwhile, the physical dissipation rate ϵ_{phy} is almost

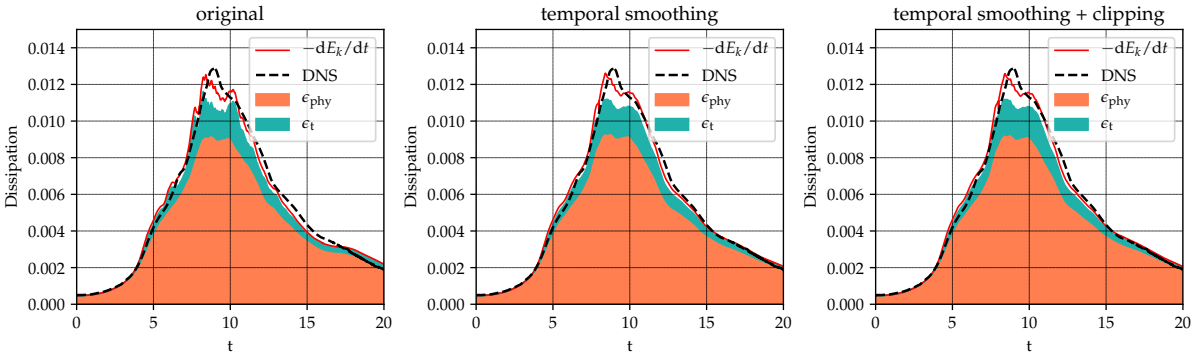

(a)

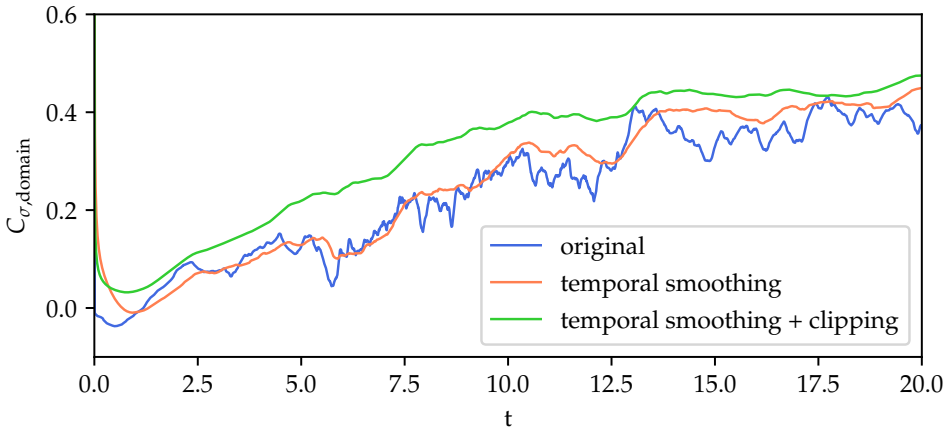

(b)

Figure 5.20: Effect of temporal smoothing: comparison of (a) dissipation distribution and (b) model constant C_σ for original and temporal smoothing simulations under $N = 16, P = 5$.

not influenced by temporal smoothing, which means that the development of turbulent structures is not affected. Once again, we see that the additional clipping treatment does not bring recognizable difference to the dissipation.

In Figure 5.20(b), the evolution of domain-averaged model constant for all three cases are presented. Although the temporal smoothing works on ν_t, we can also see the smoothing effect on C_σ where the high-frequency oscillations are filtered out while the evolution tendency remains. Besides, the start-up issue of σ-model is fixed for temporal smoothing as we see that the model constant drops rapidly at the very beginning. With additional clipping treatment, we find that the smoothness of model constant evolution is further improved, though it does not affect the simulation result remarkably.

6 Conclusion and Future Perspective

In the present work, the properties and potential of σ-model in large-eddy simulation with the discontinuous Galerkin methods are carefully analyzed. The static as well as the dynamic σ-model are validated using the Taylor-Green Vortex. We firstly argued that for higher order simulation of under-resolved turbulent flows, the no-model approach lacks of extra dissipation whereas unphysical noisy turbulent structures are observed. The dynamic σ-model brings extra turbulent dissipation in this situation and can compensate the absence of numerical dissipation. In this way, a good consistency of simulations is shown in a wide range of polynomial orders. Besides, the dynamic σ-model also exhibits rational behavior under h- and P-refinement, through which the total dissipation rate converge to the DNS reference. We also find that the cut-off polynomial order P_c can influence the approximation quality of dynamic σ-model. For lower P_c, the SGS dissipation is smoother but the noisy structures are not well dissipated. For higher P_c, the noisy structures are better dissipated while the oscillation of SGS dissipation is observed. Despite of the differences, the large-scale vortex structures of TGV flow are always reserved regarding different P_c.

For static σ-model, the model constant needs to be firstly calibrated according to the results of dynamic model. We find that although the effective spatial resolution is fixed, the model constant still changes in terms of polynomial order P, since the amount of numerical dissipation is undetermined which affect the contribution of σ-model. With calibrated model constant, the static σ-model shows good agreement with dynamic model on the dissipation behavior. Furthermore, the oscillation of SGS dissipation observed from dynamic model simulations is much improved by static model.

In the end, the performance of turbulent flow solver with implemented σ-model is investigated. We find that in general, the implementation of σ-model costs less than 20 % additional running time which is acceptable compared with the improvement it brings. Besides, some other techniques to stabilize the dynamic model, including clipping and temporal smoothing are discussed. We find that the remaining negative values of model constant are neglectable after averaging over element. Therefore, clipping them to zero cannot bring remarkable improvement on stability of dynamic model. On the other hand, the effect temporal smoothing is significant. By applying the recursive filter to the SGS viscosity, the temporal oscillations of model constant as well as SGS dissipation are removed and a better result is obtained.

Despite all the findings listed above, there are still a lot of questions to answer. Firstly, the relation between model constant and spatial discretization parameters needs to be clarified. At present, we find that the model constant is influenced by the amount of numerical dissipation, which shows a strong relevance to polynomial order P. Ideally, the model constant should remain constant with a proper definition of Δ for all h and P, which is the original intention of SGS model. Alternatively one can attempt to express model constant as function of h and P, such that the static σ-model could be

barrier-free to use. Secondly, some features of σ-model, such as its near-wall behavior cannot be evaluated via Taylor-Green Vortex flow simulations, since there is no rigid boundaries for the test case. We expect the effect of σ-model applied to turbulent channel flow problems to see its further potential combined with high-order methods. Finally, the evaluation of simulation quality in this work is mainly completed via human visual system. A filtered DNS result on the employed LES-grid is expected to give more detailed and convinced comparison.

References

[1] A. Beck, G. Gassner, and C.-D. Munz. *On the Effect of Flux Functions in Discontinuous Galerkin Simulations of Underresolved Turbulence*, volume 95, pages 145–155. 01 2014.

[2] G. Gassner and A. Beck. On the accuracy of high-order discretizations for underresolved turbulence simulations. *Theoretical and Computational Fluid Dynamics*, 27, 06 2012.

[3] N. Fehn, M. Kronbichler, C. Lehrenfeld, G. Lube, and P. Schroeder. High-order DG solvers for under-resolved turbulent incompressible flows: A comparison of L2 and H (div) methods. *International Journal for Numerical Methods in Fluids*, 91, 08 2019.

[4] M. J. Brazell, M. K. Stoellinger, and D. J. Mavriplis. *Using LES in a Discontinuous Galerkin method with constant and dynamic SGS models*.

[5] J.-B. Chapelier, M. de la Llave Plata, and E. Lamballais. Development of a multiscale LES model in the context of a modal discontinuous Galerkin method. *Computer Methods in Applied Mechanics and Engineering*, 307:275–299, 2016.

[6] H.M. Blackburn and S. Schmidt. Spectral element filtering techniques for large eddy simulation with dynamic estimation. *Journal of Computational Physics*, 186(2):610–629, 2003.

[7] F. Nicoud, H. B. Toda, O. Cabrit, S. Bose, and J. Lee. Using singular values to build a subgrid-scale model for large eddy simulations. *Physics of Fluids*, 23(8):085106, 2011.

[8] J. Fröhlich and W. Rodi. *Introduction to Large Eddy Simulation of Turbulent Flows*, page 267–298. Cambridge University Press, 2002.

[9] J. Fröhlich. *Large Eddy Simulation turbulenter Strömungen*. Vieweg+Teubner Verlag, 2006.

[10] J. W. Deardorff. The use of subgrid transport equations in a three-dimensional model of atmospheric turbulence. *Journal of Fluids Engineering*, 95(3):429–438, 09 1973.

[11] R. A. Clark. *Evaluation of Subgrid-Scale Turbulence Models Using a Fully Simulated Turbulent Flow.* PhD thesis, Stanford Univ., CA., December 1977.

[12] P. Spalart, W-H Jou, M. Strelets, and S. Allmaras. Comments on the feasibility of LES for wings, and on a hybrid RANS/LES approach. 01 1997.

[13] C.-W Shu. A brief survey on discontinuous Galerkin methods in computational fluid dynamics. *Advances in Mechanics*, 43:541–554, 11 2013.

[14] J. Stiller. A spectral deferred correction method for incompressible flow with variable viscosity. *Journal of Computational Physics*, 423:109840, 2020.

[15] N. Fehn, W. A. Wall, and M. Kronbichler. Robust and efficient discontinuous Galerkin methods

for under-resolved turbulent incompressible flows. *Journal of Computational Physics*, 372:667–693, 2018.

[16] F. van der Bos and B. J. Geurts. Computational error-analysis of a discontinuous Galerkin discretization applied to large-eddy simulation of homogeneous turbulence. *Computer Methods in Applied Mechanics and Engineering*, 199(13):903–915, 2010. Turbulence Modeling for Large Eddy Simulations.

[17] M Marek, A. Tyliszczak, and A. Boguslawski. Large eddy simulation of incompressible free round jet with discontinuous Galerkin method. *International Journal for Numerical Methods in Fluids*, 79(4):164–182, 2015.

[18] M. Germano, U. Piomelli, P. Moin, and W. H. Cabot. A dynamic subgrid-scale eddy viscosity model. *Physics of Fluids A: Fluid Dynamics*, 3(7):1760–1765, 1991.

[19] D. K. Lilly. A proposed modification of the Germano subgrid-scale closure method. *Physics of Fluids A: Fluid Dynamics*, 4(3):633–635, 1992.

[20] S. Heinz and H. Gopalan. Realizable versus non-realizable dynamic subgrid-scale stress models. *Physics of Fluids*, 24(11):115105, November 2012.

[21] M. Breuer. Large eddy simulation of the subcritical flow past a circular cylinder: numerical and modeling aspects. *International Journal for Numerical Methods in Fluids*, 28(9):1281–1302, 1998.

[22] D. Drikakis, C. Fureby, F. F. Grinstein, and D. Youngs. Simulation of transition and turbulence decay in the Taylor-Green vortex. *Journal of Turbulence*, 8:N20, 2007.

[23] Z. Wang, K. Fidkowski, R. Abgrall, F. Bassi, D. Caraeni, A. Cary, H. Deconinck, R. Hartmann, K. Hillewaert, H.T. Huynh, N. Kroll, G. May, P.-O. Persson, B. van Leer, and M. Visbal. High-order CFD methods: Current status and perspective. *International Journal for Numerical Methods in Fluids*, 72:811–845, 01 2013.

[24] J. Jeong and F. Hussain. On the identification of a vortex. *Journal of Fluid Mechanics*, 285:69–94, 1995.

[25] K. M. Hasan, P. J. Basser, D. L. Parker, and A. L. Alexander. Analytical computation of the eigenvalues and eigenvectors in DT-MRI. *Journal of Magnetic Resonance*, 152(1):41–47, 2001.

Appendix

A.1 Calculation of the singular values for σ-model

Nicoud et al. [7] suggests two methods to compute the singular values of local velocity gradient tensor, which is required by σ-model.

The first method is to employ the optimized scientific computing libraries such as LAPACK. For this idea, we need to firstly build the matrix $\boldsymbol{G} = \boldsymbol{g}^{\boldsymbol{T}}\boldsymbol{g}$, which is symmetric semi-definite positive and thus its eigenvalues are always positive. Secondly, we compute three eigenvalues of $\boldsymbol{G}$ using LAPACK and order them from large to small such that $\lambda_1 > \lambda_2 > \lambda_3$. In this way, we obtain the singular values of $\boldsymbol{g}$ as $\sigma_1 = \sqrt{\lambda_1}$, $\sigma_2 = \sqrt{\lambda_2}$, $\sigma_3 = \sqrt{\lambda_3}$, which are also ordered from large to small. Alternatively, we can directly use the DGESVD routine from LAPACK to perform a singular value decomposition (SVD) for $\boldsymbol{g}$, from which the singular values of $\boldsymbol{g}$ are obtained.

The second method developed by [25] is employed for the present work. This method is self-contained, no need of matrix operations or external libraries. The computation process is illustrated as follows

- Firstly, we need to build $\boldsymbol{G} = \boldsymbol{g}^{\boldsymbol{T}}\boldsymbol{g}$ from the velocity gradient tensor.
- Then compute the invariants of $\boldsymbol{G}$

$$\begin{aligned} \mathcal{I}_1 =& \mathrm{tr}(\boldsymbol{G}) \quad , \\ \mathcal{I}_2 =& \frac{1}{2}\left(\mathrm{tr}(\boldsymbol{G})^2 - \mathrm{tr}(\boldsymbol{G}^2)\right) \quad , \\ \mathcal{I}_3 =& \det(\boldsymbol{G}) \quad . \end{aligned} \tag{A.1}$$

- After that, we need to compute angles from the invariants

$$\begin{aligned} \alpha_1 =& \frac{\mathcal{I}_1^2}{9} - \frac{\mathcal{I}_2}{3} \quad , \\ \alpha_2 =& \frac{\mathcal{I}_1^3}{27} - \frac{\mathcal{I}_1\mathcal{I}_2}{6} + \frac{\mathcal{I}_3}{2} \quad , \\ \alpha_3 =& \frac{1}{3}\arccos\left(\frac{\alpha_2}{\alpha_1^{3/2}}\right) \quad . \end{aligned} \tag{A.2}$$

  Note that for meaningful singular values, α_1 must be positive. Otherwise, the computation procedure is terminated and no SGS viscosity is resulted. Besides, $\alpha_2/\alpha_1^{3/2}$ must be clipped into the domain of definition of $\arccos$ function $[-1,1]$ in case that the values out of domain can cause NaN (Not a Number) errors.

- The last step is to calculate the singular values from above, which are automatically ordered from large to small

$$\begin{aligned}\sigma_1 =& \sqrt{\frac{\mathcal{I}_1}{3} + 2\sqrt{\alpha_1}\cos\alpha_3} \quad , \\ \sigma_2 =& \sqrt{\frac{\mathcal{I}_1}{3} - 2\sqrt{\alpha_1}\cos\left(\frac{\pi}{3} + \alpha_3\right)} \quad , \\ \sigma_3 =& \sqrt{\frac{\mathcal{I}_1}{3} - 2\sqrt{\alpha_1}\cos\left(\frac{\pi}{3} - \alpha_3\right)} \quad .\end{aligned} \tag{A.3}$$

A.2 The λ_2-criterion

The λ_2-criterion proposed by Jeong et al. [24] is used for detection of vortex core in a three-dimensional flow. The starting point is to separate the local velocity gradient tensor $\boldsymbol{g}$ ($g_{ij} = \partial u_j / \partial x_i$) in symmetric and antisymmetric parts $\boldsymbol{S}$ and $\boldsymbol{\Omega}$

$$\begin{aligned}\boldsymbol{S} =& \frac{1}{2}\left(\boldsymbol{g}^{\boldsymbol{T}} + \boldsymbol{g}\right) \\ \boldsymbol{\Omega} =& \frac{1}{2}\left(\boldsymbol{g}^{\boldsymbol{T}} - \boldsymbol{g}\right) \quad .\end{aligned} \tag{A.4}$$

Next step is to calculate the three eigenvalues of $\boldsymbol{S}^2 + \boldsymbol{\Omega}^2$ which are ordered form large to small, e.g. $\lambda_1 > \lambda_2 > \lambda_3$. A point belongs to a vortex core, if and only if at least two of three eigenvalues are negative, e.g. $\lambda_2 < 0$. Therefore, the iso-surface of $\lambda_2 = 0$ remarks the boundary of a vortex tube with $\lambda_2 < 0$. For practical reasons, we always use a smaller λ_2, such as $\lambda_2 = -1.5$, to exclude noisy structures, which makes the visualization of vortex structures clear and legible.

Acknowledgments

At this point, I would like to express my gratitude to all the related personnel who support me during my Diplomarbeit and learning in Dresden.

Particularly, I want to thank Prof. Jochen Fröhlich and Professur für Strömungsmechanik for giving the chance to fulfill my passion of computational fluid dynamics with this challenging project.

I want to thank my supervisors, Dr. Jörg Stiller and Ms. Martina Grotteschi for their careful and helpful guidance during my work, which enables me to keep learning and pushing my work forward, even in this special period of global pandemic.

Last but not least, I want to thank Mr. Andreas Hauffe and Zentrum für Informationsdienste und Hochleistungsrechnen for providing the computational environment and resources.

Selbstständigkeitserklärung

Hiermit erkläre ich, dass ich die von mir am heutigen Tag der Professur für Strömungsmechanik eingereichte Diplomarbeit zum Thema

Adaptation and validation of the σ-model for large-eddy simulations with the discontinuous Galerkin method

vollkommen selbstständig verfasst und keine anderen als die angegebenen Quellen und Hilfsmittel benutzt, sowie Zitate kenntlich gemacht habe.

Dresden, 15. Juni 2021

Yang Liu